Evaluation of a Total Energy-Rate Sensor on a Transport Airplane

Aaron J. Ostroff,
Richard M. Hueschen,
R. F. Hellbaum,
Christine M. Belcastro,
and J. F. Creedon

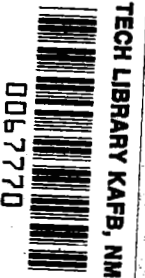**25**

25th Anniversary
1958-1983

NASA

NASA
Technical
Paper
2212

1983

Evaluation of a Total Energy-Rate Sensor on a Transport Airplane

Aaron J. Ostroff,
Richard M. Hueschen,
R. F. Hellbaum,
Christine M. Belcastro,
and J. F. Creedon

Langley Research Center
Hampton, Virginia

SUMMARY

   This paper describes an evaluation of a sensor that measures the total energy
rate of an airplane relative to the airstream. The sensor consists of two cylin-
drical probes in the airstream. Each probe has a small orifice located on the down-
stream side of the cylinder, an in-line acoustic filter, and a pressure-sensing
altitude-rate transducer. A sensor using just one probe was originally developed and
flight-tested for application to soaring flight, and has also been evaluated for
powered flight with the probe mounted on a boom in the free airstream. For this
evaluation, two probes were located on the forward fuselage of a small commercial jet
transport and were subjected to body-induced flow disturbances.

   A potential application for the sensor is in display and control systems
designed to reduce glide-slope deviations during wind-shear penetration. Time-
history data comparisons between the measured data and calculated values show suffi-
ciently good agreement to warrant research into potential applications.

   Sections of this paper include the sensor description and experimental config-
uration, frequency response tests, analytical sensor model development, and flight-
test results in the form of time-history plots for several aircraft maneuvers.

INTRODUCTION

   A sensor that measures the rate of change of airplane total energy with respect
to the airstream has previously been developed and analyzed. A main component of
this sensor is a cylindrical probe that is inserted into the airstream. The probe
contains a small orifice located on the downstream side of the cylinder, and thus
provides a pressure source sensitive to both static and dynamic pressure. The rela-
tionship of the pressure measurement to total energy (potential plus kinetic) is
shown in the appendix.

   References 1 to 5 present information relating to the construction and analysis
of the probe and to a potential soaring flight application for using the probe to
measure total energy rate. The initial total energy-rate sensor combined the probe
with a variometer, which produced an electrical signal proportional to the time rate
of change of input pressure, and was tested on a sailplane (refs. 1 and 3). The
simplicity of this sensor and its ability to measure the change in energy with
respect to the airstream led to further interest for application to powered aircraft
flight. Since wind shear causes changes in airspeed, and hence changes in kinetic
energy, one potential application is to use the sensor output for display or control
systems designed to reduce the effects of wind shear on final approach. Typical
aircraft devices that have been used to detect wind shear are reported in refer-
ences 6 to 8. In reference 6, it is concluded that the output of a total energy-rate
sensor could be displayed on a total energy-rate indicator, in a flight director, or
in an electronic attitude-director indicator. Furthermore, the sensor might be used
as part of an automatic flight control system since the sensor provides leading indi-
cations of changes in descent rate or flight-path angle in response to wind shears.
These applications are considered as follow-on research and are not part of this
paper.

The sailplane sensor was modified to include an in-line acoustic filter and was evaluated on a De Havilland DHC-6 Twin Otter airplane (ref. 9). The energy probe was mounted on a nose boom, where it was relatively free from body-induced flow-field effects. The airplane was instrumented with an inertial platform, an air data system, body-rate sensors, and a data recording system. The recorded variables were used to make an independent calculation of the airplane total energy rate. Excellent comparisons between calculated and measured values of total energy-rate were obtained.

Elements of the sensor evaluation described in this paper (fig. 1) include the probe, an in-line acoustic filter, and an altitude-rate transducer, as opposed to a variometer as used in the Twin Otter sensor evaluation. The altitude-rate transducer senses the filtered probe absolute pressure, converts the pressure into an electrical signal representing altitude by using a standard atmosphere function, and produces the time rate of change of this signal as an output. The output is thus proportional to total energy rate.

The Twin Otter flight-test results demonstrated the sensor measuring capability with the probe located in the free airstream. In the current research, however, an objective was to evaluate the capability of the sensor to measure the total energy rate during flight with the probes located on the fuselage of a small commercial transport airplane, where they are exposed to body-induced flow disturbances. For this evaluation, one probe was mounted on each side of the airplane, and the pressures were either combined to make one measurement or used to make two independent simultaneous measurements for comparison.

The evaluation approach described in this report was to judge qualitatively whether the measured sensor values of total energy rate and the calculated values of total energy rate derived from independent instrument systems on the airplane compare well enough to warrant further research into possible applications. This approach allowed time-varying comparisons during a number of flight maneuvers. A determination of specific sensor accuracy numbers was not a goal of this research.

Various airplane maneuvers performed in the sensor evaluation are described in this paper. Other sections of the paper include the physical description of the system, the calibration procedure, the analytical model, and flight-test results, with comparisons of the total energy-rate data with energy rate derived by calculations using data recorded by the instrumentation.

SYMBOLS

C_p pressure coefficient

d_α lateral distance from x-z plane of airplane to α vane (positive to right), m

g acceleration due to gravity, m/s^2

H_k specific kinetic energy, or kinetic energy per unit weight, m

$\dot{H}$ specific total energy rate, m/s

$\dot{H}_{kf}$ filtered time rate of change of specific kinetic energy, m/s

$\dot{H}_p$ airplane altitude rate derived from complementary filter, m/s

$\dot{H}_{pf}$ filtered time rate of change of specific potential energy, m/s

h altitude, m

$\dot{h}$ altitude rate, m/s

h_β perpendicular distance from x-y plane of airplane to β vane (positive down), m

l_α longitudinal distance from airplane y-z plane to α vane (positive forward), m

l_β longitudinal distance from airplane y-z plane to β vane (positive forward), m

M Mach number

P_e unfiltered pressure measurement on energy probe, Pa

P_o sea-level static pressure, Pa

P_s measured static pressure, Pa

$\Delta P_1, \Delta P_2, \Delta P_3$ pressure measurements used during checkout, Pa

p measured roll rate, rad/s

q measured pitch rate, rad/s

$\bar{q}$ dynamic pressure, Pa

q_c measured impact pressure, Pa

r measured body-axis yaw rate, rad/s in equations, deg/s in figures

s Laplace variable, s^{-1}

T_o sea-level static air temperature, K

T_s static temperature at altitude, K

$T(s)$ transfer function for sensor filtering

T_t total air temperature measurement, K

V_o true airspeed, m/s

$V_{x,b}$ inertial velocity, longitudinal axis, m/s

$V_{x,o}$ longitudinal component of true airspeed, m/s

$V_{x,w}$ wind velocity, longitudinal axis, m/s

w_1, w_2 characteristic frequencies representing altitude rate transducer and acoustic filter, rad/s

α angle of attack, deg

α_m measured angle of attack, rad

α_o airplane angle of attack, radians in equations, degrees in figures

β angle of sideslip, deg

β_m measured angle of sideslip, rad

β_o airplane angle of sideslip, radians in equations, degrees in figures

γ specific-heat ratio of air, 1.4

η recovery factor of total temperature, 1.0

θ measured pitch attitude of airplane, deg

ρ rotation of energy probe in y-z plane, rad

ρ_o sea-level density, kg/m^3

ρ_s measured static air density, kg/m^3

ϕ measured roll attitude of airplane, deg

Superscripts:

L   left energy probe

R   right energy probe

SENSOR DESCRIPTION AND EXPERIMENTAL CONFIGURATION

The total energy-rate sensor was evaluated on a transport airplane that was being used for terminal-area-operations research. The airplane was instrumented for recording flight conditions and other necessary parameters.

As shown in figures 2 and 3, energy probes were mounted on the back of the lower-left and upper-right pitot-static tube mounts. The probes have a vertical separation of approximately 61 cm. The probes are oriented 20° from the plane that is normal to the airstream. These locations were chosen because (1) flow asymmetries should cancel when the diametrically opposite probes are vented together; and (2) the dual pitot-static tube set was instrumented on the airplane. Wind-tunnel data indicated that, with the energy probes mounted as described, the effects on the accuracy of the airspeed and altitude measurements obtained from the pitot-static tube were negligible.

A detailed analysis of the total energy probe is contained in references 1 to 5. The total-energy-probe measurement is a function of a coefficient of pressure C_p. This coefficient is defined as the difference between measured and static pressure

normalized by the dynamic pressure (see appendix), and is characterized in the above references as a measure of performance. References 3 and 5 contain data from various wind-tunnel experiments. Plotted results show the variation in C_p as a function of probe forward sweep angles and sideslip angles, and as a function of physical parameters such as probe diameter, orifice diameter, probe length, distance from center of orifice to the tip of the probe, and various bent-probe configurations.

The reference data show that a probe forward sweep angle of approximately 20° with respect to the flow direction insures relative insensitivity of C_p to changes in airplane angle of attack. For this forward sweep angle, C_p is nearly constant (-1.0) around the aft side of the cylinder over a wide range of Reynolds numbers. The most critical dimension is the distance from the orifice center to the tip of the probe. Setting this distance to twice the probe diameter has given the best results. A typical range for the probe diameter is between 0.48 cm (3/16 in.) and 0.64 cm (1/4 in.).

Figure 4 is a schematic diagram of the instrumentation package installed on the test airplane, and figure 5 is a photograph of the instrumentation package. Two system configurations were studied - a separate probe configuration and a combined probe configuration. Either configuration could be selected by the appropriate position of a solenoid selector valve. In the separate configuration, the energy probes were independent. Each probe had its own filter volume and altitude-rate transducer. In the combined configuration, the pressures from both restrictors were directed by the solenoid selection valve to the right filter volume. Therefore, the output signal from the right altitude-rate transducer was a combination of the left and right probe pressure inputs. For this configuration, the left filter volume and altitude-rate transducer were inactive.

To obtain accurate pressure measurements for use in postflight calculations of total energy rate using independent sensors, two pressure transducers with an accuracy of ±1 Pa and a range of 100 000 Pa were used on the instrumentation package. One transducer measured the static pressure P_s sensed by the two pitot-static tubes on which the energy probes were mounted, and the other transducer measured the impact pressure q_c sensed by the lower left pitot-static tube. Both of these measurements were used to calculate airspeed. Other pressure transducers were included on the instrumentation package to record auxiliary pressure data. These data were not needed for the independent calculation of total energy rate, but were needed for possible use in identifying sources of malfunction or unexplained data anomalies. The auxiliary data included the left unfiltered energy probe pressure P_e^L, the differential pressure between the left and right probes ΔP_3, and the pressure drops across the two acoustic filters ΔP_1 and ΔP_2. An analysis of the auxiliary data was not required for this report, so no further mention of it will be made.

Other airplane sensors and systems (not part of the instrumentation package of fig. 5, but used for the postflight calculation of total energy rate) include body-rate gyros, alpha and beta vanes, an inertial platform, and the air data computer. Roll, pitch, and yaw rate measurements were obtained from the gyros, the angle of attack and sideslip from the vanes, and the total air temperature from the air data computer. A measure of the vertical velocity $\dot{h}_p$ was obtained from a complementary filter in the flight control computer. The filter inputs were barometric altitude rate, from the air data computer, and vertical acceleration, from the inertial platform.

For the analysis of maneuvers which encountered wind-shear disturbances, additional measurements were used. These measurements were roll, pitch, and true-heading attitude from the inertial platform, and north and east inertial velocities computed in the inertial navigation system.

Barometric altitude from the air data computer was used for data plots in this report as an aid in illustrating the test maneuvers of the airplane, but was not used in any calculations.

The sensors are part of the airplane research system being used to develop advanced displays and automatic flight controls. The measurements obtained from these sensors are generally of better quality than those obtained from existing transport airplanes. However, there is no precise measurement available that is traceable to the National Bureau of Standards, such as the measurement of weight and length. Air data sensors such as the pitot-static tubes and vanes are subject to flow disturbances over the fuselage which can introduce errors into the measurements. In addition, the angle-of-attack sensor accuracy is dependent on airplane flap setting, but this measurement should have only a small effect on the results of the calculations.

FREQUENCY RESPONSE TESTS

A frequency response test was conducted on the total-energy-probe sensor to determine a representative transfer function for use in the analytical model. Oscillating pressures generated by a small speaker were amplified by a combination of fluidic amplifiers and were applied to the energy probes. Electrical signals corresponding to both the input pressures and the altitude-rate transducer outputs were recorded on a multichannel oscillograph. By employing the solenoid switch (fig. 4), both the left and right sensors could be tested independently, or the pressures could be applied simultaneously to both probes to test the combined sensor.

Two oscillating pressure amplitudes were used in each configuration, since previous laboratory tests showed that the acoustic-filter break frequencies changed with the input signal amplitude. The peak-to-peak sinusoidal amplitude for the low-level pressure input was approximately 40 Pa, and the peak-to-peak high-level pressure input was 660 Pa. At sea level, these pressures correspond to altitude changes of 3.4 m and 50 m, respectively. Transfer functions for each of the four conditions described were constructed by approximating break frequencies from the frequency response plots obtained from the data recorded on the oscillograph. These transfer functions $T(s)$ are as follows:

$T(s)$ for –	
Low level	High level
Separate systems	
$\dfrac{9.42s}{(s + 0.625)(s + 2.32)(s + 6.49)}$	$\dfrac{9.52s}{(s + 0.400)(s + 2.50)(s + 9.52)}$
Combined systems	
$\dfrac{12.4s}{(s + 1.25)(s + 2.65)(s + 3.75)}$	$\dfrac{10.4s}{(s + 1.00)(s + 2.15)(s + 4.85)}$

where s represents the Laplace variable.

The lowest frequency pole in the above functions is contributed by the acoustic filter, and the two higher-frequency poles and the differentiator term are contributed by the altitude-rate transducer. All gains have been normalized in the expressions.

A single approximate transfer function for each sensor configuration was desired. The highest frequency pole was discarded to simplify the filter approximation, because it was expected to have a negligible effect on the signals of interest. The approximate transfer function was then determined for the combined system using the average value of the two remaining corresponding poles of the high- and low-level transfer functions. For the separate-system approximate model, the altitude-rate transducer pole was selected to be the same value as that used in the combined system, but the acoustic-filter pole was selected to be one-half that of the combined system, since the parallel restrictors are now separated.

The approximate transfer function used in the analytical model section is

$$T(s) = \frac{w_1 w_2 s}{(s + w_1)(s + w_2)} \tag{1}$$

with frequencies w_1, w_2 shown in the following table:

	w_1, rad/s	w_2, rad/s
Combined system	1.13	2.40
Separate system	.56	2.40

Figures 6 and 7 show a comparison of the transfer function approximation with the measured data. Figures 6(a) and 6(b) contain the amplitude and phase responses, respectively, for the separate-system configuration, and figures 7(a) and 7(b) represent those for the combined system. The experimental data are plotted both with and without the differentiator. The differentiator term is extracted because it does not affect the characteristic equation. Only the low signal-level data are presented, but similar results can be shown for the high signal-level cases. The worst-case differences appear at the higher frequencies and are particularly evident in the phase-angle plots. This is because of the deletion of the high frequency pole in the transfer function approximation.

SENSOR ANALYTICAL MODEL

The evaluation technique used in reference 9 and in this paper is to compare the sensor total energy-rate measurement with an independent calculation of total energy rate. The necessary variables were measured in-flight and were combined in post-flight processing to make the calculation using the analytical model developed in this section. To make valid time-history comparisons, the analytical model must have the same filtering characteristics as the sensor. This is accomplished by using the transfer functions developed in the preceding section. A secondary reason for the

analytical model development is the use of the analytical model for potential follow-up applications.

Equations that model the combined system are simpler than those for the separate system, because flow irregularities resulting from lateral airplane motions tend to offset each other since pressure sources from opposite sides of the airplane are tied together. As expected, the separate-system configuration was found to be very sensitive to sideslip activity. Therefore, an approximation has been added to the equations to account for sideslip.

Combined-System Equations

Aircraft measurements of static pressure P_s, impact pressure q_c, and total air temperature T_t are used in the calculation of true airspeed V_o. The equations used are as follows:

$$M = \sqrt{\frac{2}{\gamma - 1}} \sqrt{\left(\frac{q_c}{P_s} + 1\right)^{(\gamma-1)/\gamma} - 1} \tag{2}$$

$$T_s = \frac{T_t}{1 + \left(\frac{\gamma - 1}{2}\right)\eta M^2} \tag{3}$$

$$\rho_s = \frac{T_o}{T_s} \frac{P_s}{P_o} \rho_o \tag{4}$$

$$V_o = M\sqrt{\gamma \frac{P_s}{\rho_s}} \tag{5}$$

where M is the Mach number, T_s is the static temperature at altitude, η is the total-temperature probe recovery factor (approximately 1.0 from ref. 10), T_o is the sea-level static air temperature, P_o is the sea-level static pressure, ρ_o is the sea-level density, and γ is the ratio of specific heat of air (1.4). Values for T_o, P_o, and ρ_o are taken from reference 11.

The longitudinal component of true airspeed $V_{x,o}$ was calculated by using measurements of angle of attack α_m and angle of sideslip β_m, with corrections for sensor locations. These corrections are usually negligible, but have given slightly better transient responses during some of the maneuvers. The equations leading to the calculation for $V_{x,o}$ are as follows (ref. 12):

$$\alpha_o = \alpha_m - (pd_\alpha - q l_\alpha)/V_o \tag{6}$$

8

$$\beta_o = \beta_m - (r\iota_\beta - ph_\beta)/V_o \tag{7}$$

$$V_{x,o} = V_o \cos \alpha_o \cos \beta_o \tag{8}$$

In equations (6) to (8), p, q, and r represent the measured airplane roll, pitch, and yaw body-axis rates; ι, h, and d represent moment arms from the vehicle center of gravity in the longitudinal, vertical, and lateral directions, respectively; the subscripts o, α, and β refer to the center of gravity and the α and β vanes; and the subscript m refers to the measured angles.

Kinetic energy H_k relative to the airstream is a function of true airspeed V_o. In reference 9, $V_{x,o}$ was used since the total energy probe is fixed to the airplane and since this quantity showed better comparison with the measured signal for large values of α_o and β_o.

Similar results were found in the present test-flight evaluation, and even though the difference is insignificant in most cases, $V_{x,o}$ is used in the analytical model as

$$H_k = (V_{x,o})^2/2g \tag{9}$$

where g represents the acceleration due to gravity. Equation (9) is a calculation for specific energy, or energy per unit weight, and has units of height (see appendix). In this paper, as in references 6 and 9, energy and energy height are used synonymously.

There are two first-order filters that require modeling, as described in the section "Frequency Response Tests." One filter represents the altitude-rate transducer, which has a pole w_2 at 2.4 rad/s. The other first-order filter represents the acoustic-filter (restrictor-volume) combination, which, for the combined system, has a pole w_1 at 1.13 rad/s, and for the separate system is one-half that value (0.56 rad/s).

The equation for filtered kinetic energy rate is

$$\dot{H}_{kf} = \frac{w_1 w_2 s}{(s + w_1)(s + w_2)} H_k \tag{10}$$

A similar equation is used to calculate the filtered potential-energy rate $\dot{H}_{pf}$. A differentiation is not required since the input was derived from a complementary filter on the aircraft (ref. 13). The equation for filtered potential-energy rate is

$$\dot{H}_{pf} = \frac{w_1 w_2}{(s + w_1)(s + w_2)} \dot{H}_p \tag{11}$$

9

and the total energy rate $\dot{H}$ is the summation of equations (10) and (11) as follows:

$$\dot{H} = \dot{H}_{kf} + \dot{H}_{pf} \tag{12}$$

Separate-System Equations

An approximation has been made to $V_{x,o}$ in equation (8) to account for sideslip sensitivity and the angular orientation of each energy probe. Changing the notation in equation (8) to $\bar{V}_{x,o}$ the modified equation for $V_{x,o}$ becomes

$$V_{x,o} = \bar{V}_{x,o}(1 - 0.5 \sin \rho \sin \beta_o) \tag{13}$$

Using superscript L for the left probe ($\rho = -90°$) and superscript R for the right probe ($\rho = 90°$),

$$V_{x,o}^{L} = \bar{V}_{x,o}(1 + 0.5 \sin \beta_o) \tag{14a}$$

$$V_{x,o}^{R} = \bar{V}_{x,o}(1 - 0.5 \sin \beta_o) \tag{14b}$$

The coefficient 0.5 is an empirical value that was found to give reasonable dynamic results for the aircraft maneuvers considered in this paper. Kinetic energy is calculated for each probe separately by substituting equations (14a) and (14b) into equation (9). All other equations are identical to those for the combined systems.

FLIGHT TESTS

The purpose of the test flights was to gather data which could be used to compare the total energy-rate sensor measurements with those computed from independent measurements of the onboard instrumentation. The purposes of the prescribed aircraft maneuvers were to produce desired energy changes, such as a potential and kinetic exchange, and to establish flow conditions that could conceivably cause erroneous outputs from the energy probe, especially in the separate-system configuration. The maneuvers were accomplished by means of manual pilot control and automatic control modes on the research test aircraft. The automatic modes employed were calibrated airspeed hold (CAS), velocity control wheel steering (VCWS), which is control about the command airplane velocity vector, attitude control wheel steering (ATTCWS), which is control about the command pitch and roll attitudes, and flight-path angle hold (FPA). Data were gathered for eight specified test maneuvers which are summarized in table 1. The conditions achieved and maneuvers performed in flight deviated only slightly from those of the table.

TABLE 1.- SUMMARY OF TEST MANEUVERS

Test maneuver	Initial airspeed, m/s	Initial altitude, m	Flap/initial control modes	Notes
Take-off	0	0	15°/manual	Standard take-off to 762 m
Potential and kinetic exchange	67	914	25°/CAS, VCWS	Disengage CAS; command 30° descent flight-path angle followed by 3° climb
Kinetic change	129	762	0°/CAS, FPA	Decrease speed to 69 m/s with speed brakes; increase with speed brakes down; flaps selected according to schedule
Potential change	77	914	15°/CAS, VCWS	While in CAS hold, begin with 5° descent flight-path angle; at 305 m go to 5° climb
Roll	67	762	40°/VCWS	Left (-30°) to right (30°) roll at level altitude
Pitch	67	762	40°/ATTCWS	Pitch up from trim by 10° followed by -5° pitch
Sideslip	67	762	40°/ATTCWS	Half-rudder inputs to full-rudder inputs left and right
Landing	64	457	40°/manual	Manual landing; approximately 5555 m final

RESULTS

This section contains a discussion of the time history plots of each flight-test maneuver for the combined system and the separate system. Comparisons are made between the total energy-rate values recorded from the sensor during the flight tests and the postflight calculated values. The calculated values were determined from independent measurements recorded during the flight tests using the equations described in the section "Sensor Analytical Model."

Figures 8 to 16 represent results from the combined-system maneuvers. Each figure contains plots of the variables significant to that test. The bottom three plots in each figure always show $\dot{H}_{pf}$, $\dot{H}_{kf}$, and $\dot{H}$. Calculated values of $\dot{H}$ are shown by a solid line, and measured values of $\dot{H}$ are shown by a dashed line. The altitude h plots show step changes of approximately 25 m due to the data recorder resolution. This plot is shown only to help illustrate the flight-test maneuver, and the data on this plot were not used in any of the analytical model calculations.

11

Take-Off

Figure 8 represents a take-off with the data starting approximately 4 to 5 seconds prior to lift-off. The lift-off time is illustrated in both the h and the H_{pf} plots. At the initial time, the pitch rotation has already begun as illustrated in the θ plot. Airspeed increased from an initial 60 m/s to 115 m/s when data recording was terminated. The altitude-rate transducer has a linear signal range of ±16 m/s and is seen to saturate at approximately 7 seconds into the run. A good comparison between calculated and measured $\dot{H}$ signals can be seen during the first 7 seconds. At several intervals during the 60-second run, the measured $\dot{H}$ dropped below the saturated level. The calculated $\dot{H}$ also decreased below the saturated level during the same time periods, although much more than the measured value. Larger differences occurred in this time period, possibly because of sensor saturation, but the trends of the sensor and calculated values are the same.

Potential and Kinetic Energy Exchange

Figure 9 represents a potential and kinetic energy exchange. During this run, V_o increased from 66 to 97 m/s, resulting in a positive $\dot{H}_{kf}$, and h decreased from 900 to 555 m, resulting in a negative $\dot{H}_{pf}$. Total energy remains relatively constant during the first 50 seconds of the maneuver, as indicated by the near-zero average value of $\dot{H}$. During the last 40 seconds of this run, there are increased wind gusts, with a possible wind shear taking place at approximately 60 seconds; the wind shear is discussed in more detail later in this section. The $\dot{H}$ plot shows that the wind disturbance upsets the energy exchange maneuver and generally results in a loss of total energy. In spite of the gusts, a good correlation exists between measured and calculated $\dot{H}$ values. At times, the calculated $\dot{H}$ appears to have a slightly faster response than the measured $\dot{H}$; this is also evident on some of the other plots. The differences in the $\dot{H}$ curves suggest that the time constant and phase lag of the approximated transfer function were slightly smaller than those of the sensor.

Kinetic Energy Change

Figure 10 represents the results of a kinetic energy change maneuver. The airspeed decreased from 130 m/s to 72 m/s, and altitude was held relatively constant by the autopilot, as shown by H_{pf}. At approximately 90 seconds, the pilot advanced the throttles for maximum thrust and manually lowered the speed brakes, causing V_o to increase. Some change in potential energy occurred at this point, as illustrated in the $\dot{H}_{pf}$ plot, mainly because of the sudden increased lift due to lowering the speed brakes (spoilers).

During the last 13 seconds, the level of airplane acceleration resulted in sensor saturation. Agreement between the $\dot{H}$ time histories is not as good as it is in most of the other tests. The larger differences may be due to larger errors in the pitot-static measurements because of the larger angles of attack encountered for this maneuver. At 77 to 78 seconds, α_o was at stall angle of attack; however, the general trend between calculated and measured $\dot{H}$ appears to be maintained.

Potential Energy Change

A potential energy change is illustrated in figure 11. During this run, the pilot commanded a 5° descent angle to the autopilot, causing h to decrease at a rate of approximately 3.5 m/s, and the autopilot was commanded to maintain a constant calibrated airspeed. At approximately 48 seconds, the V_o plot shows a sudden decrease in the airspeed and then a gradual increase as the autopilot attempts to maintain the commanded airspeed. The sudden decrease in airspeed was caused by a possible wind shear and is discussed in more detail later in this section. Although there appears to be differences in the phase and response characteristics of the calculated and measured $\dot{H}$ curves, their shapes are in good agreement for this maneuver, including the time of the sudden decrease in airspeed.

Roll and Pitch Maneuvers

A roll maneuver and a pitch maneuver are illustrated in figures 12 and 13, respectively. For the roll maneuver, the pilot commanded bank attitudes of ±30° using the autopilot, which was also commanded to maintain level flight. Level flight was essentially maintained, as shown by the $\dot{H}_{pf}$ curve, and the desired bank angles were achieved. For the pitch maneuver, the pilot commanded a 15° pitch-up followed by a 5° pitch-down. Both commands were relative to level-flight attitude ($\approx 3°$ pitch). The $\dot{H}$ curves show good correlation for both maneuvers in spite of possible flow-field changes caused by the airplane motions. Larger differences in $\dot{H}$ are generally noted when sideslip β_o is larger for the roll maneuver and when the angle of attack α_o is larger for the pitch maneuver.

Sideslip Maneuver

The sideslip maneuver was executed by the pilot using manual rudder inputs and is illustrated in figure 14. The maneuver deviated from the test plan, but suitable data were still recorded for analysis. The β_o curve shows sideslip angles up to 6.4° during the initial and final portions of the plot, and a sideslip of -9.7° during the 60- to 70-second time interval. Airspeed V_o and altitude h were relatively constant and the bank angle ϕ (not shown) was held near zero by the autopilot during this run. The yaw rate r is included in this figure to help illustrate time rates of change in β_o. The average values of $\dot{H}$ are near zero, as illustrated by both the calculated and measured curves. As is shown subsequently in the discussion of the separate-system results, the individual energy probes are very sensitive to sideslip activity. For the most part, the combined system tends to average out sideslip sensitivities of the individual probes. The good agreement of the $\dot{H}$ curves for this run suggests that the larger differences, noted for the roll maneuver where sideslip was present, may be due to roll attitude and roll rate, rather than sideslip.

Landing

Figure 15 shows results of a completely manual landing maneuver. The run starts while the airplane is banked at -26° (ϕ curve) to capture the localizer. At 16 seconds, the localizer is captured and the airplane proceeds down the glide slope at a sink rate of approximately 3 to 4 m/s. Airspeed V_o decreases slightly between 25 and 60 seconds, and an average loss in kinetic energy is shown by the $\dot{H}_{kf}$ plot during this time.

As illustrated by the θ plot in figure 15, flare starts at approximately 120 seconds. The main wheels touch the ground at approximately 135 seconds, and the aircraft pitches down with the nose gear touching about 5 seconds later. During the final 20 seconds of the run, the aircraft is losing airspeed as it proceeds down the runway. Overall, the calculated and measured values of $\dot{H}$ show very good agreement except when the airplane is banked at approximately 10 seconds into the run. The larger discrepancy while banked is in agreement with the results of the roll maneuver and the suggested results of the previous sideslip maneuver discussion.

Wind-Shear Analysis

The V_o and $\dot{H}$ plots in figures 9 and 11 indicate possible wind-shear encounters at the point where a sudden decrease occurs in V_o. A different set of altitude data than that plotted for the previous discussions was used to investigate and analyze these possible wind-shear encounters. Although these altitude data had more resolution, they were not used originally because they were more difficult to obtain from the recorded flight. Also, altitude data were not required for the analytical model; therefore, the source easiest to obtain was used in the prior analyses. The approach used to determine whether wind shear was present was to find the difference between inertial and airspeed components referenced to the airplane body axes. The body-axis longitudinal component of inertial velocity $V_{x,b}$ was determined by rotating the Earth-referenced velocity components ($\dot{H}_p$ and north and east velocities) to the body axes using an Euler transformation and recorded attitude data. The wind component $V_{x,w}$ is then calculated by subtracting the inertial and airspeed components of velocity as follows:

$$V_{x,w} = V_{x,b} - V_{x,o}$$

where $V_{x,o}$ is calculated as in equation (8).

Figure 16 shows the velocity components $V_{x,b}$, $V_{x,o}$, and $V_{x,w}$ and altitude h. The plots on the left-hand side show the 50- to 70-second time period from figure 9. The data show that the sudden decrease in airspeed is due to a decreased head wind as the altitude decreased. This decreased airspeed resulted in a decreased kinetic energy rate. The plots on the right-hand side of figure 16 represent the 40- to 60-second time period of figure 11 and also show that the decreased airspeed is due to a decreased head wind. When the decrease in airspeed occurs, the autopilot advances the throttle to return the airspeed to the commanded value. This analysis indicates that wind shears did occur and that the total energy-rate sensor measured the change in total energy resulting from their presence. Analysis of these test results suggests that further investigations into applications of the sensor in automatic control systems designed to alleviate adverse effects of wind shear should be conducted.

Separate Systems

Figures 17 to 23 show results of the separate-system runs. Curves on the left-hand side of each figure represent selected airplane variables (α_o, β_o, V_o, h, θ, r, and ϕ); curves on the right-hand side represent calculated values of $\dot{H}_{pf}$,

$\dot{H}^L_{kf}$, and $\dot{H}^R_{kf}$, and both calculated and measured values of $\dot{H}^L$ and $\dot{H}^R$. The super-scripts represent the left-side (L) and right-side (R) energy probe systems. The same type maneuvers that were shown previously are also shown for the separate-system flights, except for take-off, since the altitude-rate transducers again went into saturation.

The separate-system configuration shows sensitivity to sideslip maneuvers. Figure 22 illustrates the results as β_o is varied between 6.3° and -8.5°. During each change in magnitude of sideslip, as shown in the β_o and r data, the two sensors indicate total energy-rate changes that are opposite in direction with approximately the same magnitude as shown by the $\dot{H}^L$ and $\dot{H}^R$ data. These test data clearly illustrate the sideslip sensitivity of the separate-sensor configuration and show why the combined system is relatively insensitive to sideslip (fig. 14). The calculated $\dot{H}^L$ and $\dot{H}^R$ curves in figure 22 illustrate that the analytical-model sideslip approximation in equation (14) allows a rough prediction of each sensor measurement.

Figure 23 shows a 70-second time period during landing. At approximately 40 seconds, the $\dot{H}_{pf}$ data indicate increasing altitude. The reason is that the airplane was below the glide slope; therefore, the pilot commanded a pitch-up maneuver to recapture the desired flight path. As shown in the $\dot{H}^L$ and $\dot{H}^R$ plots, both energy probe sensors show reasonably good comparison with calculated values.

In general, the correlations between measured and calculated values of $\dot{H}$ are not as good as those for the combined system, and in the case when dynamic changes are occurring in the sideslip, the left and right probe outputs can be quite differ-ent. The use of a separate system for a control system application may be possible if the measurement is not of prime importance in the application and if reduced per-formance is tolerable. The separate sensor is not recommended for potential appli-cations, except to possibly fill the role as a backup sensor in case one side of the combined system fails.

CONCLUSIONS

A flight test has been made to evaluate the configuration and operation of a total energy-rate sensor on a transport airplane. One probe was located on each side of the airplane fuselage with a 20° forward sweep angle. Evaluations were made of two separate systems and one combined system that uses the average of the probe pres-sures. The evaluations were made under conditions of several airplane maneuvers. Analytical models, developed for both separate and combined systems, were used to calculate total energy-rate values, derived from independent airplane measurements, for comparison with data measured by the total energy-rate sensor. Specific conclu-sions, based upon flight test evaluation, are as follows:

1. Comparisons between sensor-measured total energy-rate data and calculated values for the combined system show sufficiently good results to warrant investiga-tions and research into potential applications of the sensor.

2. Flight-test results obtained for the combined-system configuration are supe-rior to those of the separate-systems configuration. For the mounting location chosen, the separate-system measurements were shown to be generally unsatisfactory

because of sideslip sensitivity. Therefore, their use in potential applications is not recommended, except to possibly fill the role as a backup sensor in case one side of a combined system fails. Success in such a role would depend on the importance of the sensor in the application and the amount of performance degradation that is tolerable.

3. An investigation into two of the test maneuvers shows that the total energy-rate system responds to energy changes due to wind shear. These results suggest that further investigations into applications of the sensor in automatic control systems designed to alleviate adverse effects of wind shear should be conducted.

Langley Research Center
National Aeronautics and Space Administration
Hampton, VA 23665
September 13, 1983

RELATIONSHIP BETWEEN TOTAL ENERGY RATE AND INPUT PRESSURE

The equation for total energy E is the sum of the potential energy and kinetic energy

$$E = mgh + \frac{1}{2} mV^2 \tag{A1}$$

where m is the airplane mass, g is the acceleration due to gravity, h is the altitude, and V is the airspeed of the airplane since kinetic energy relative to the airstream is being measured. Normalizing by the airplane weight, the specific energy or energy per unit weight is

$$H = h + V^2/2g \tag{A2}$$

and the time rate of change of specific energy is

$$\dot{H} = \dot{h} + V\dot{V}/g \tag{A3}$$

where $\dot{V}$ is the time rate of change of V. Flow at the orifice of the total energy probe is characterized by a coefficient of pressure defined (refs. 1 to 6) as

$$C_p = \frac{P_e - P_s}{\bar{q}} \tag{A4}$$

where P_e is the pressure at the energy probe orifice, P_s is the static pressure, and $\bar{q}$ is the dynamic pressure. Wind-tunnel tests (refs. 3 and 5) have established that the value of C_p is approximately -1.0 around the aft side of the probe for the range of Reynolds number and alignment angles used in the application of the probe to current flight parameters. With $C_p = -1.0$, equation (A4) is written as

$$P_e = P_s - \bar{q} \tag{A5}$$

Static pressure varies nonlinearly with altitude; however, for small altitude changes the time rate of change in static pressure can be represented as

$$\dot{P}_s = -\rho_s g\dot{h} \tag{A6}$$

APPENDIX

where ρ_s is the static air density. The dynamic pressure varies as the square of the airspeed

$$\bar{q} = \frac{1}{2}\rho_s V^2 \qquad (A7)$$

and the time rate of change in dynamic pressure is

$$\dot{\bar{q}} = \rho_s V\dot{V} \qquad (A8)$$

Substituting equations (A6) and (A8) into the derivative of equation (A5) yields

$$\dot{P}_e = -\rho_s g\dot{h} - \rho_s V\dot{V} \qquad (A9)$$

and normalizing by $-\rho_s g$ results in the time rate of change of specific energy (total energy rate) shown in equation (A3).

REFERENCES

1. Nicks, Oran W.: A Simple Total Energy Sensor. Soaring, vol. 40, no. 9, Sept. 1976, pp. 30-32.

2. Nicks, Oran W.: How To Make a Total Energy Sensor. Soaring, vol. 41, no. 3, Mar. 1977, pp. 23-24.

3. Nicks, Oran W.: A Simple Total Energy Sensor. NASA TM X-73928, 1976.

4. Nicks, Oran W.: Aircraft Total Energy Sensor, U.S. Pat. 4,061,128, Dec. 6, 1977.

5. Nicks, Oran W.: Further Developments in Simple Total Energy Sensors. Science and Technology of Low Speed and Motorless Flight, Perry W. Hanson, compiler, NASA CP-2085, Pt. I, 1979, pp. 219-245.

6. Joppa, Robert G.: Wind Shear Detection Using Measurement of Aircraft Total Energy Change. NASA CR-137839, 1976.

7. Rek, Bron: Windshear Indication Systems. Flight Int., vol. 116, Sept. 22, 1979, pp. 984-986.

8. Greene, R. A.: The Effects of Low-Level Wind Shear on the Approach and Go-Around Performance of a Landing Jet Aircraft. [Preprint] 790568, Soc. Automot. Eng., Apr. 1979.

9. Ostroff, Aaron J.; Hueschen, Richard M.; Hellbaum, R. F.; and Creedon, J. F.: Flight Evaluation of a Simple Total Energy-Rate System With Potential Wind-Shear Application. NASA TP-1854, 1981.

10. Kayton, Myron; and Fried, Walter R., eds.: Avionics Navigation Systems. John Wiley & Sons, Inc., c.1969.

11. U.S. Standard Atmosphere, 1962. NASA, U.S. Air Force, and U.S. Weather Bur., Dec. 1962.

12. Gainer, Thomas G.; and Hoffman, Sherwood: Summary of Transformation Equations and Equations of Motion Used in Free-Flight and Wind-Tunnel Data Reduction and Analysis. NASA SP-3070, 1972.

13. Flight Critical Control Laws for the NASA Terminal Configured Vehicle. D6-32669, Boeing Commercial Airplane Co., [1975].

AIRFLOW

20°

FUSELAGE SKIN

NORMAL TO SKIN

ENERGY PROBE

RESTRICTOR

FILTER
VOLUME

ALTITUDE-RATE
TRANSDUCER
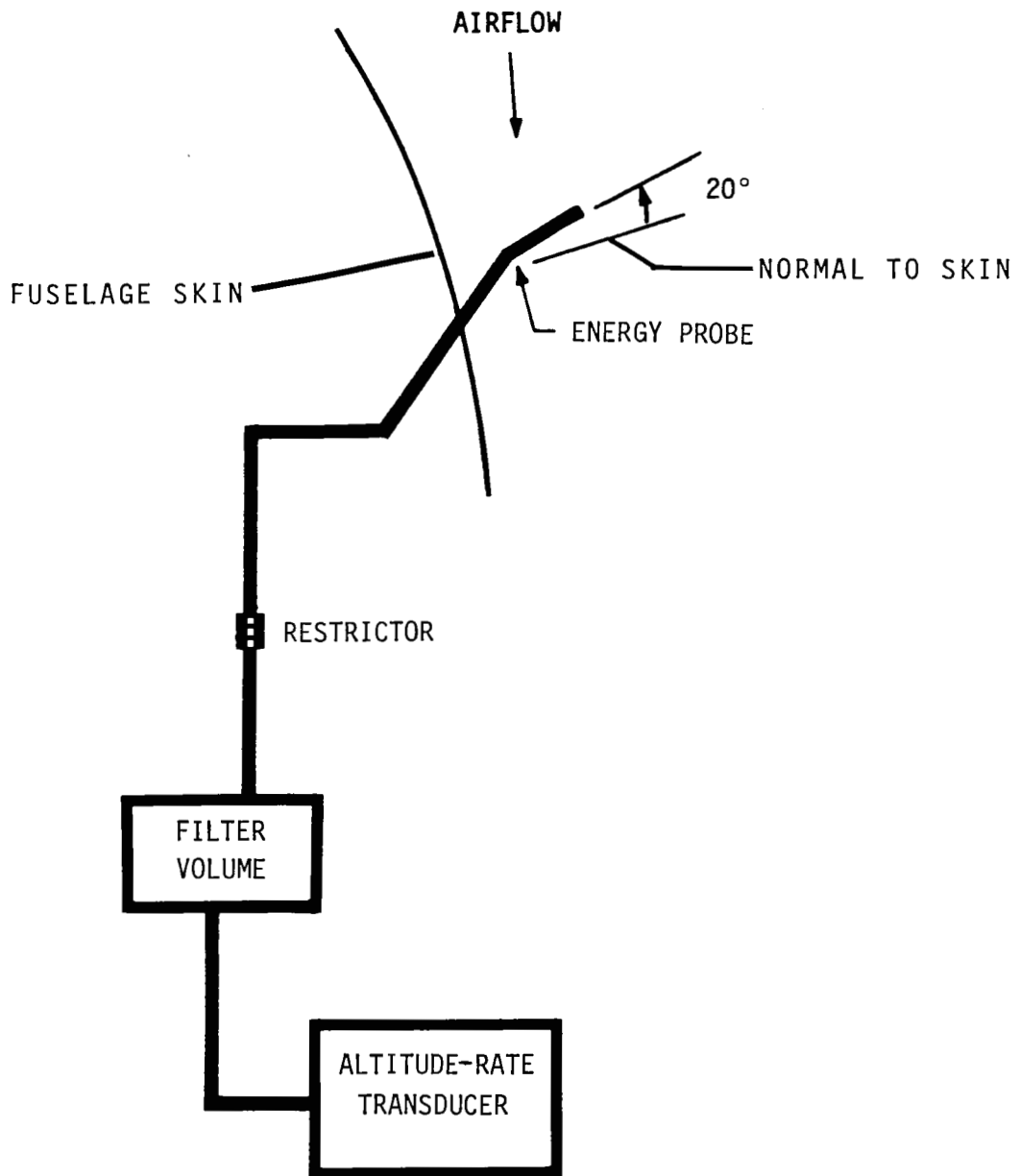
Figure 1.- Elements of total energy-rate sensor.

UPPER-RIGHT
ENERGY PROBE

PITOT-STATIC
TUBE

20°

20°

LOWER-LEFT
ENERGY PROBE

PITOT-STATIC TUBE

FUSELAGE

TOP VIEW

UPPER-RIGHT
ENERGY PROBE

61 CM

PITOT-
STATIC TUBE

LOWER-LEFT
ENERGY PROBE

PITOT-STATIC TUBE

FRONT VIEW
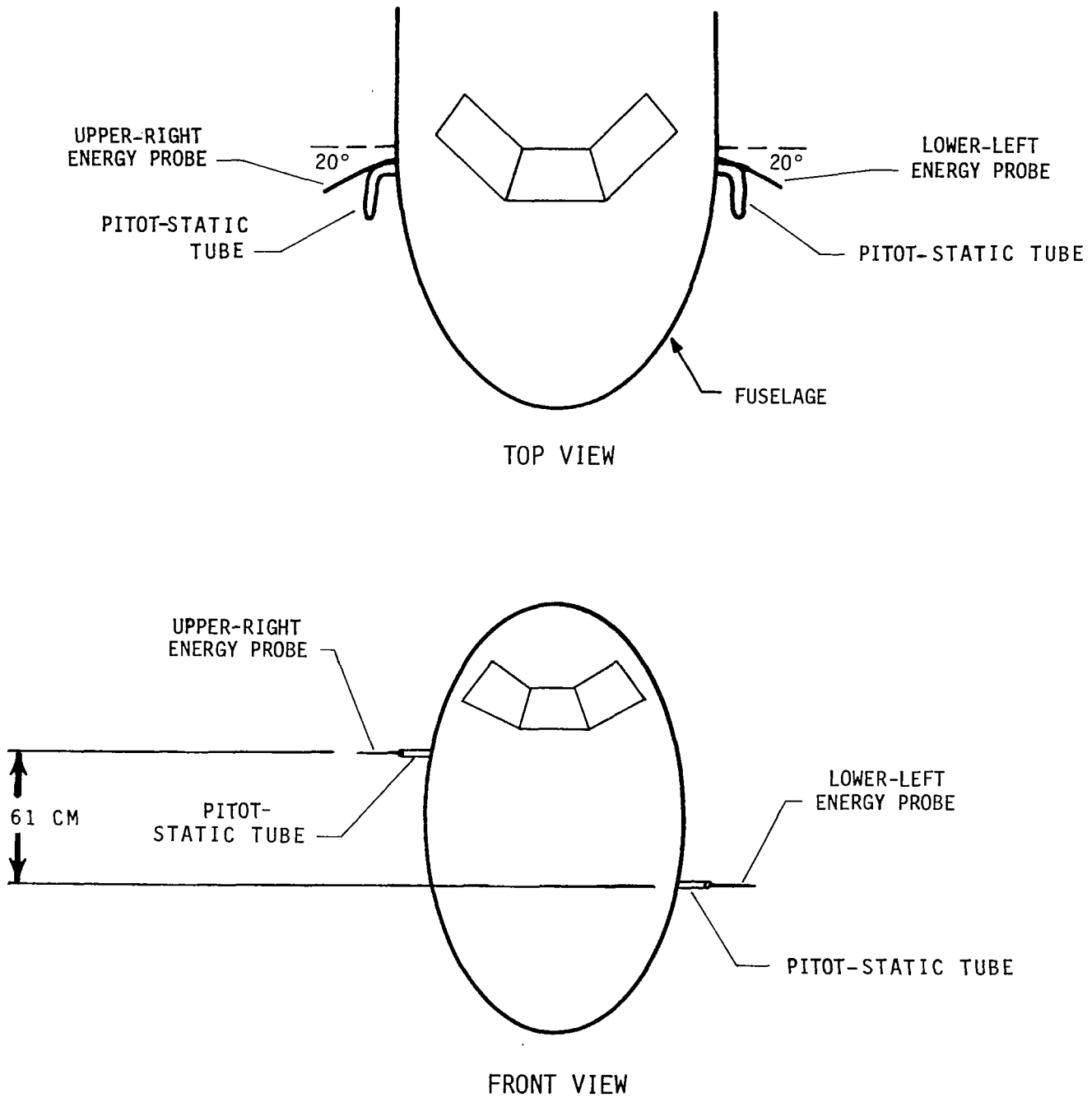
Figure 2.- Sketch of energy probe configuration on airplane.

1.27 cm

0.16-cm-diam DRILL THRU;
1-ORIFICE HOLE ON DOWNSTREAM
SIDE OF 0.64-cm o.d. TUBE

13.7 cm

ENERGY PROBE

PITOT-STATIC TUBE

20°

FUSELAGE SKIN
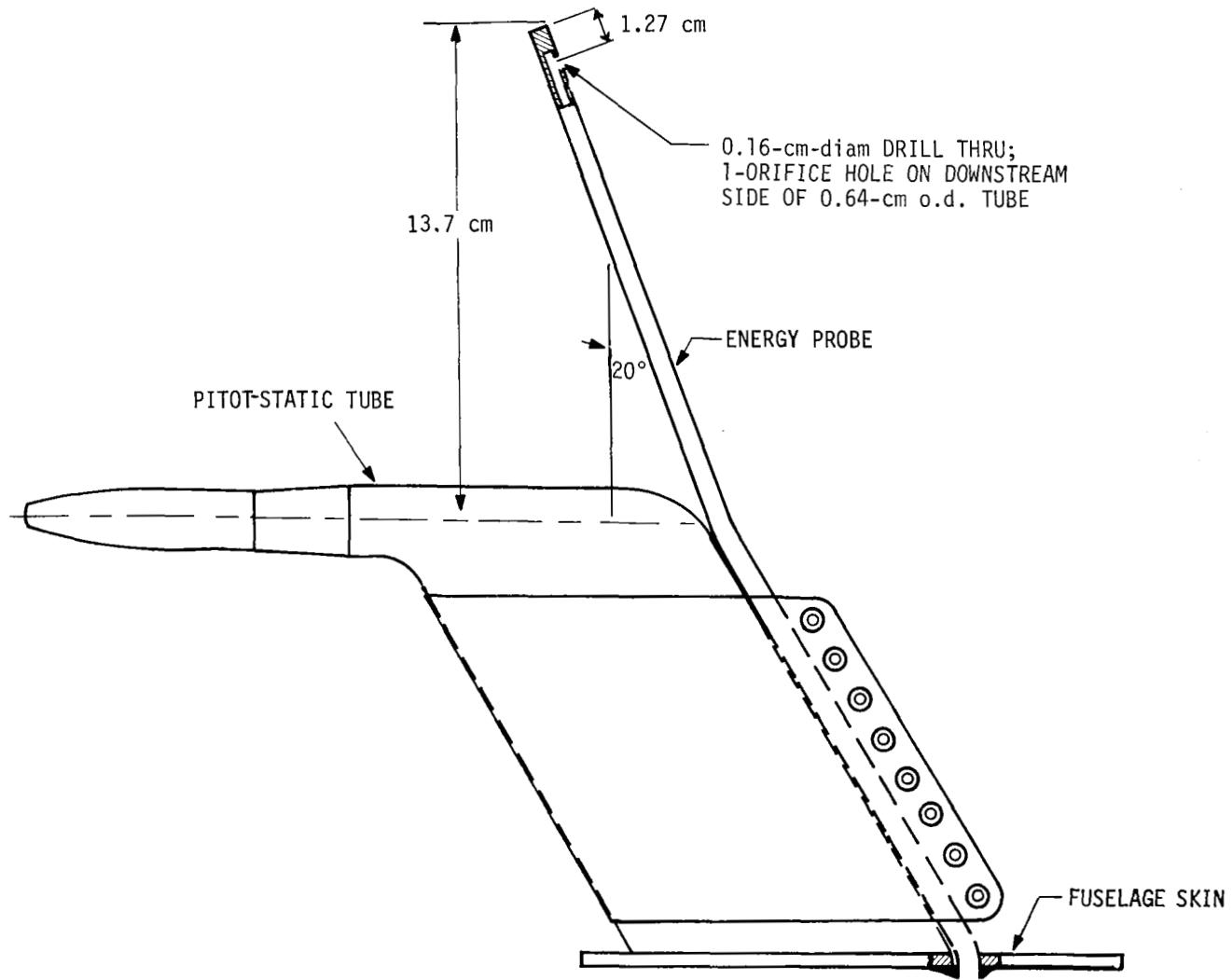
Figure 3.- Energy probe mounted on pitot-static tube.

AIRFLOW

AIRFLOW

20°

20°

ENERGY PROBE
ON LOWER-LEFT
PITOT-STATIC
TUBE

ENERGY PROBE
ON UPPER-RIGHT
PITOT-STATIC
TUBE

IMPACT
PRESSURE
TRANSDUCER
q_c

STATIC
PRESSURE
TRANSDUCER
P_s

ΔP_3

LEFT
ENERGY PROBE
PRESSURE, P_e^L

RESTRICTORS

ΔP_1

ΔP_2

SOLENOID
SELECTOR VALVE*

FILTER
VOLUME

FILTER
VOLUME

LEFT
ALTITUDE-RATE
TRANSDUCER

RIGHT
ALTITUDE-RATE
TRANSDUCER
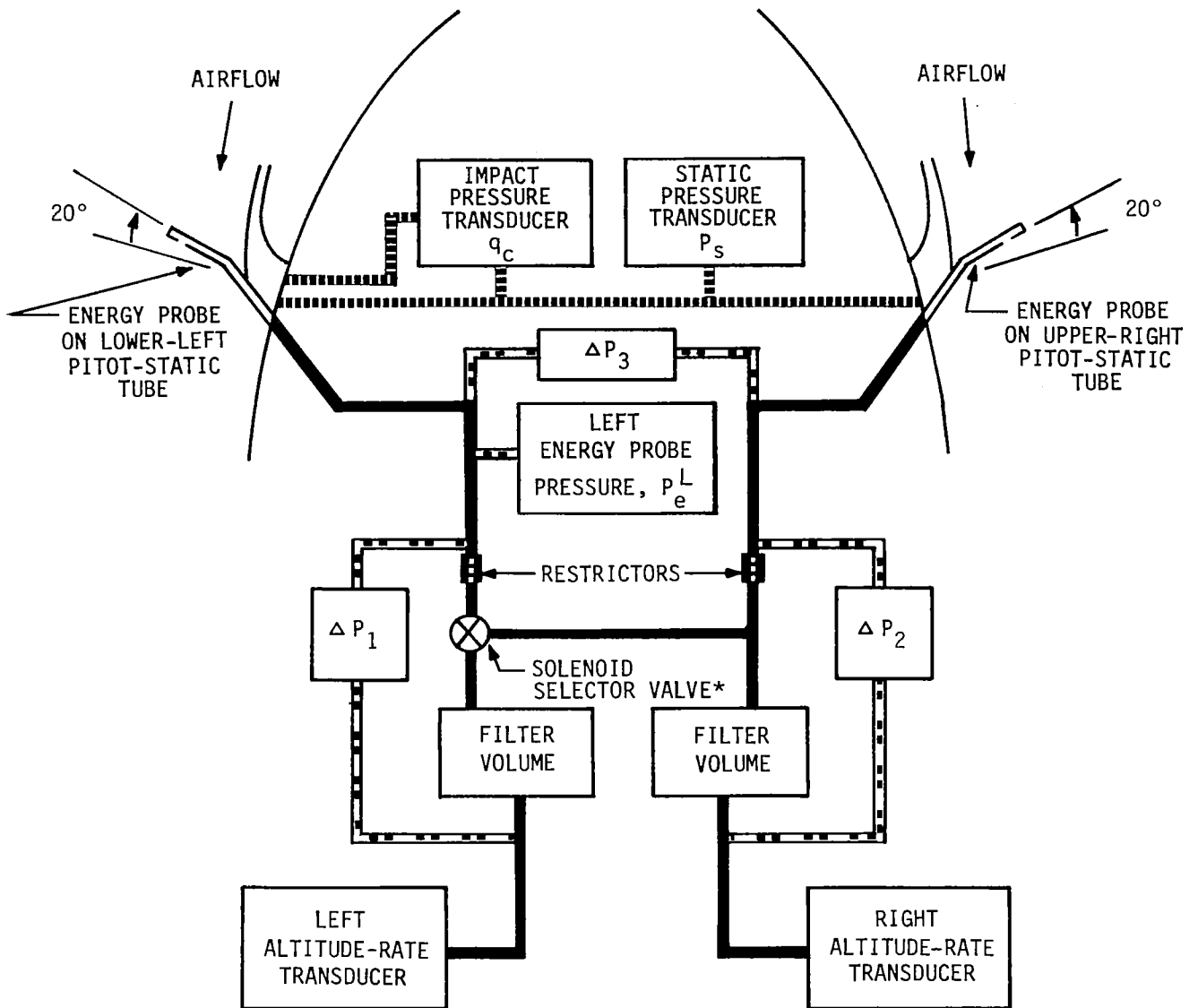
*   SELECTOR VALVE CONNECTS LEFT ENERGY PROBE TO EITHER LEFT OR
        RIGHT ALTITUDE-RATE TRANSDUCER

▪▪▪▪▪ MEASUREMENTS USED IN DATA ANALYSIS

▄▬▄ AUXILIARY MEASUREMENTS FOR SYSTEM VERIFICATION

▬▬▬ ENERGY PROBE SYSTEM

Figure 4.- Energy probe/instrumentation system.

23
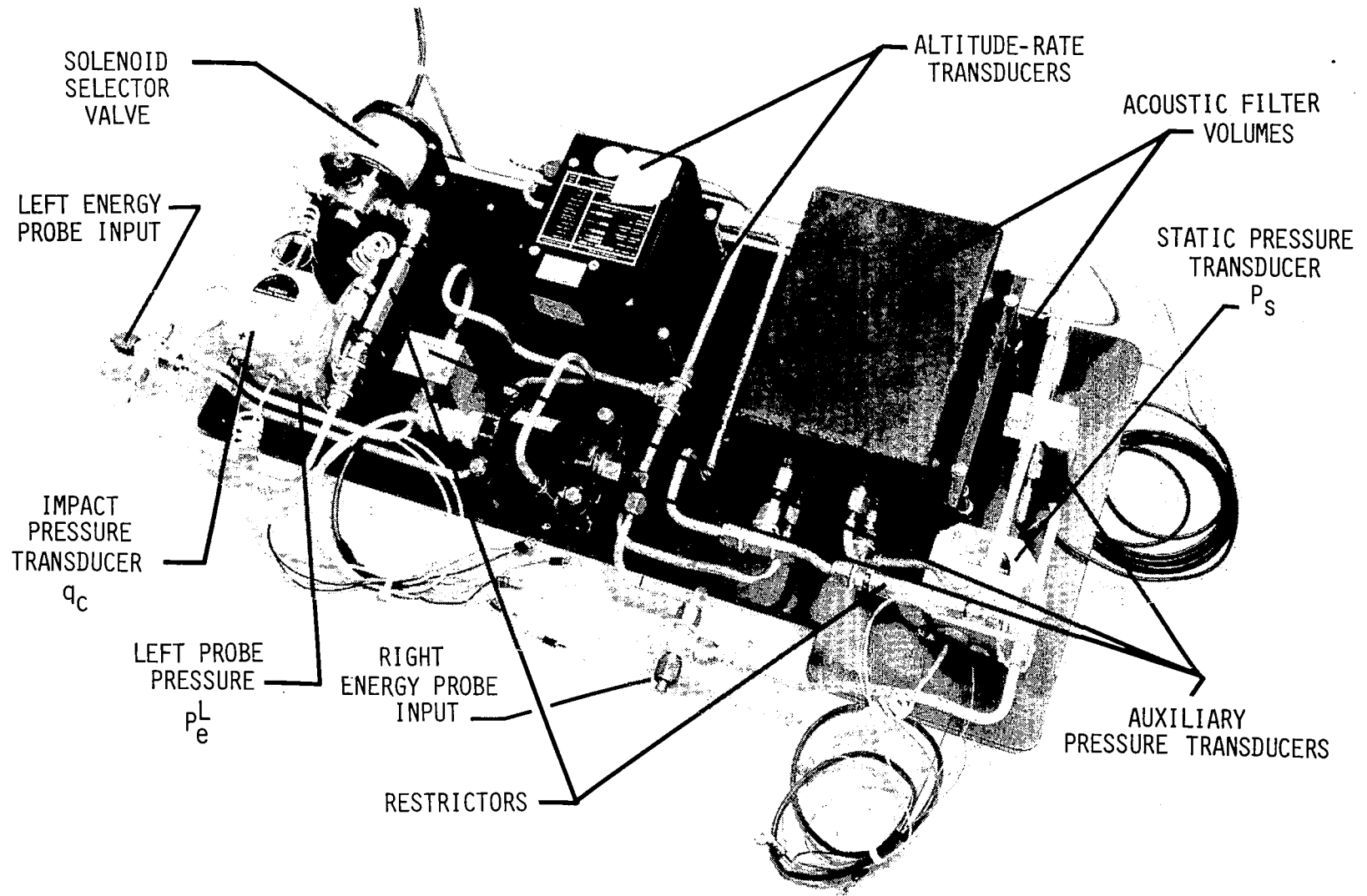
Figure 5.- Instrumentation package.

L-83-112
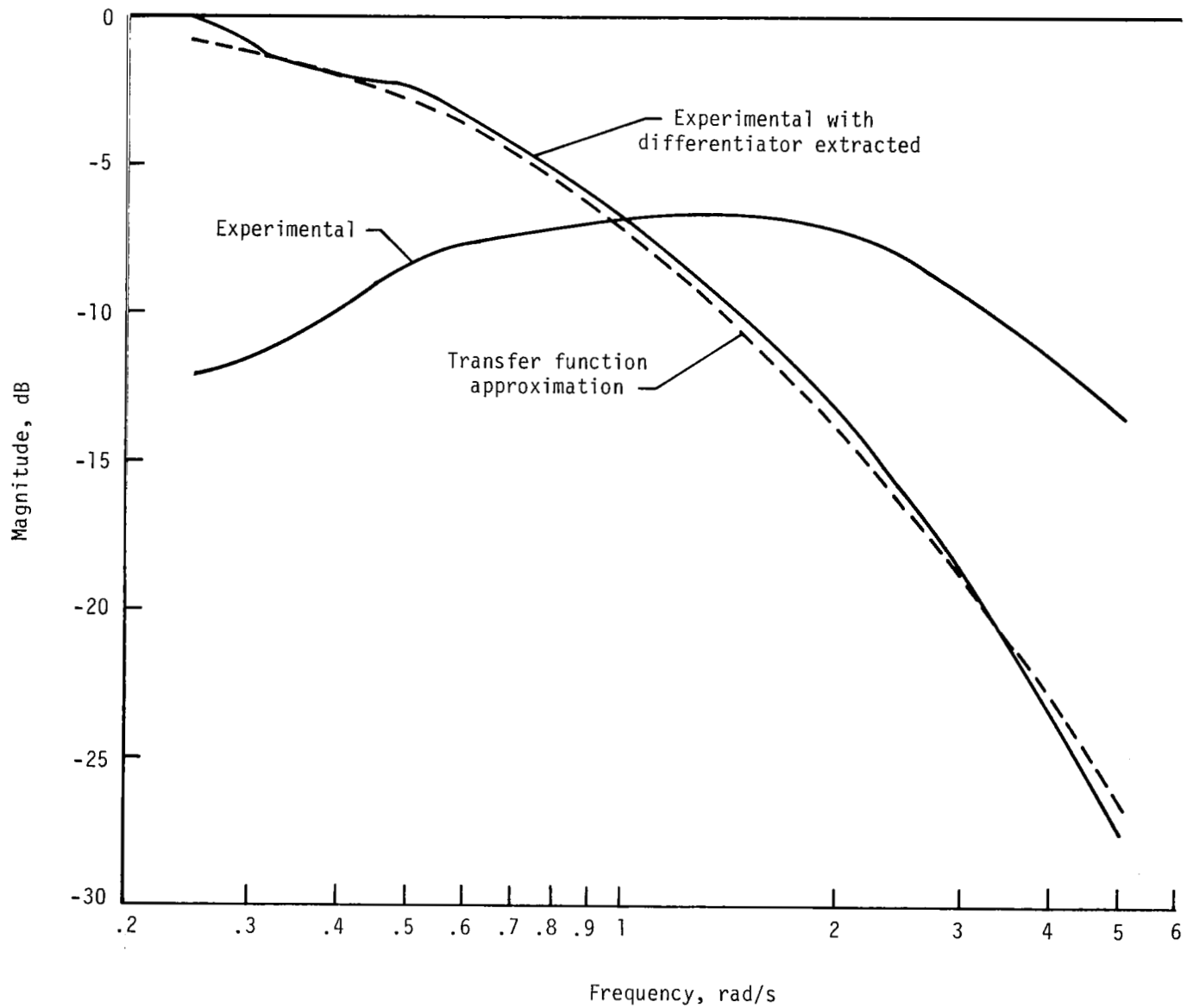
(a) Amplitude.

Figure 6.- Frequency response for separate systems.
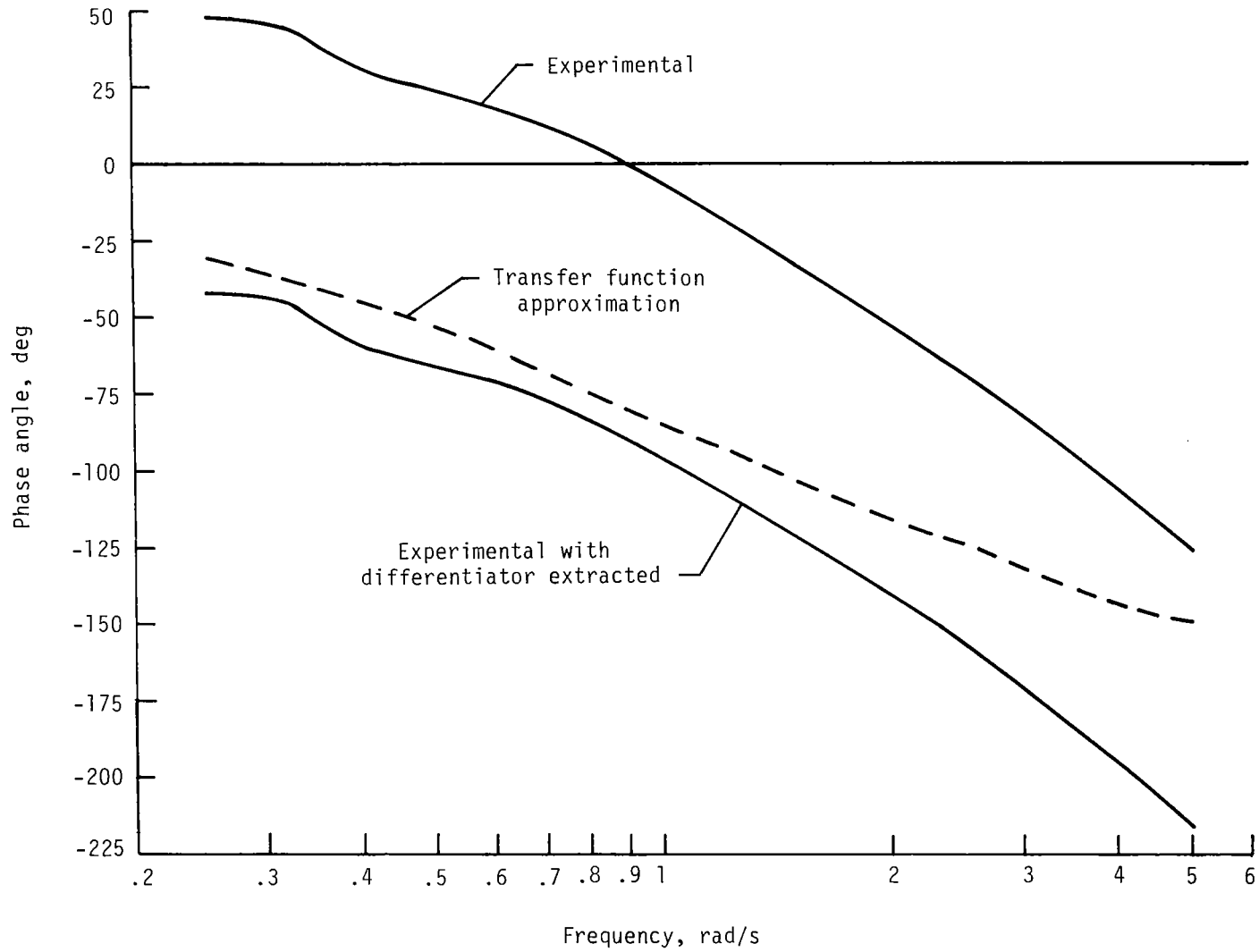
(b) Phase.

Figure 6.- Concluded.
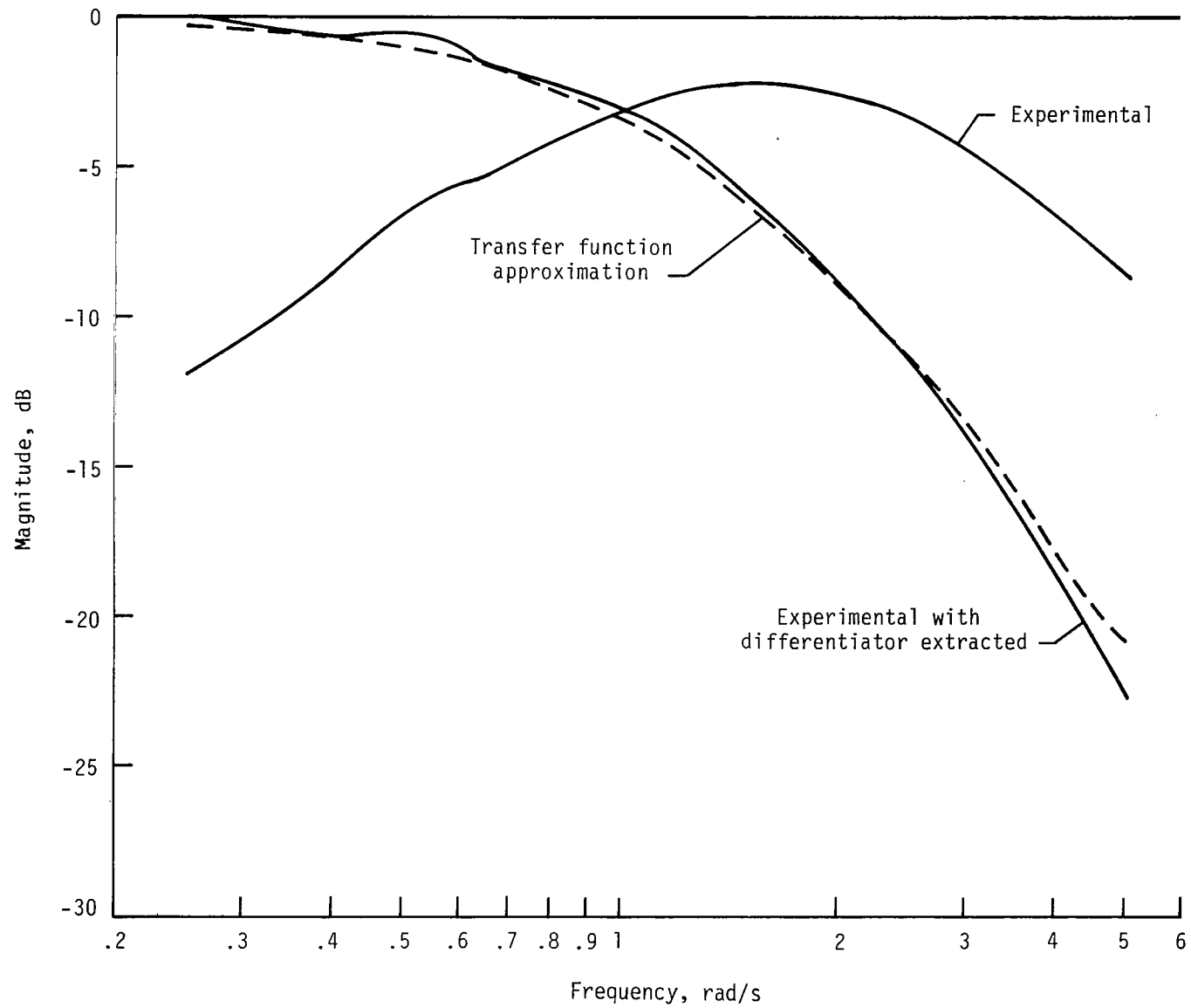
(a) Amplitude.

Figure 7.- Frequency response for combined system.
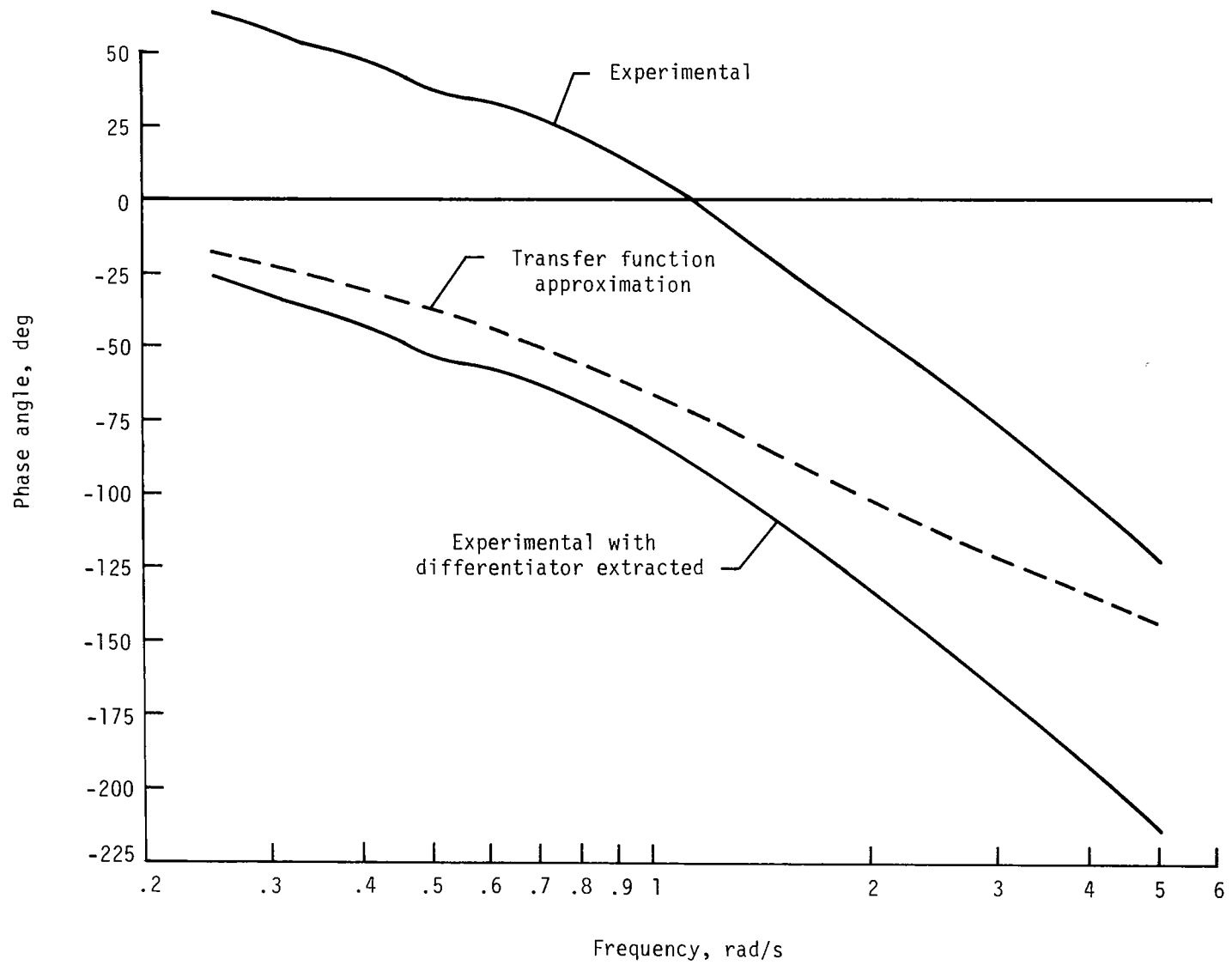
(b) Phase.

Figure 7.- Concluded.
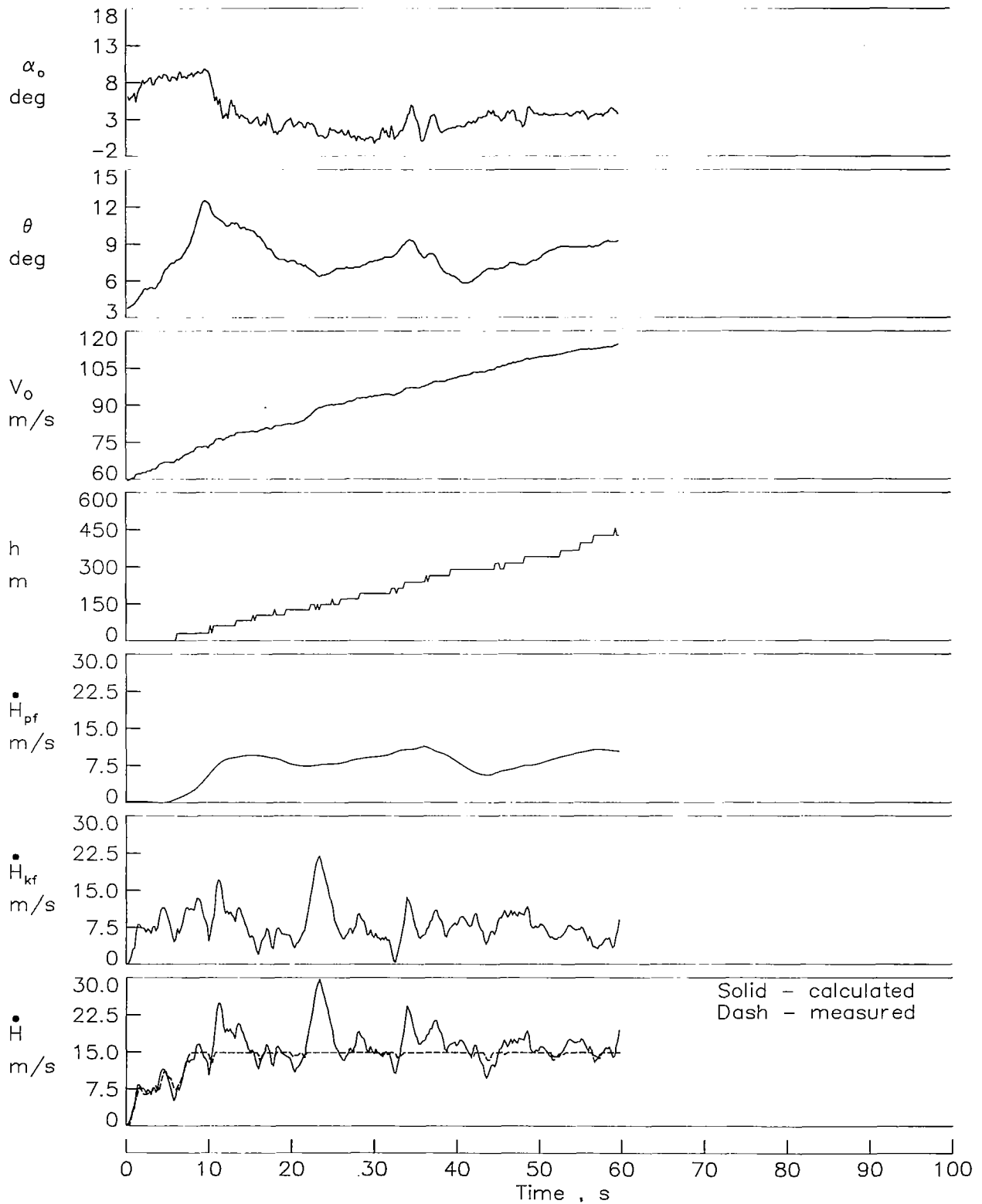
Figure 8.- Test data for combined system during take-off.
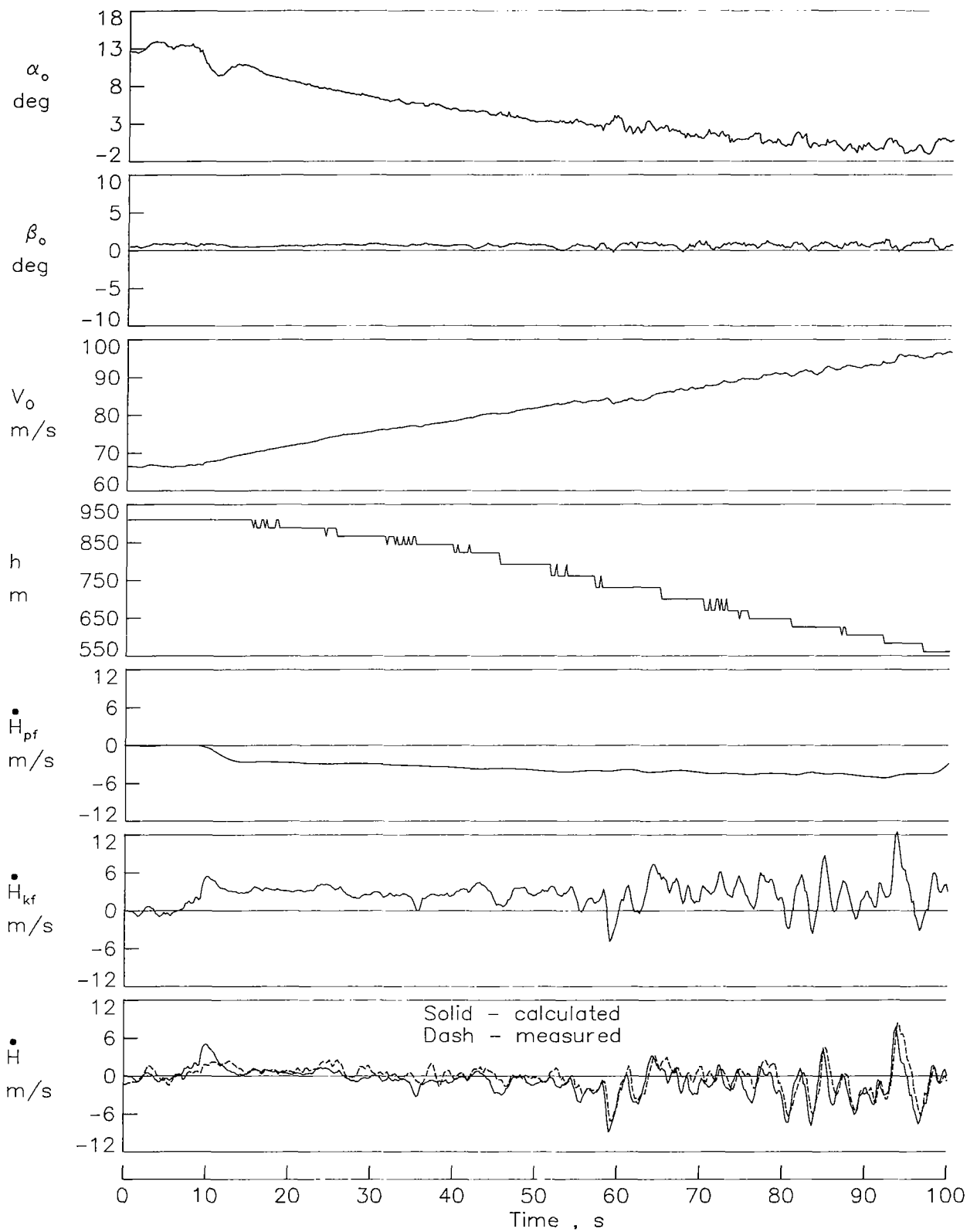
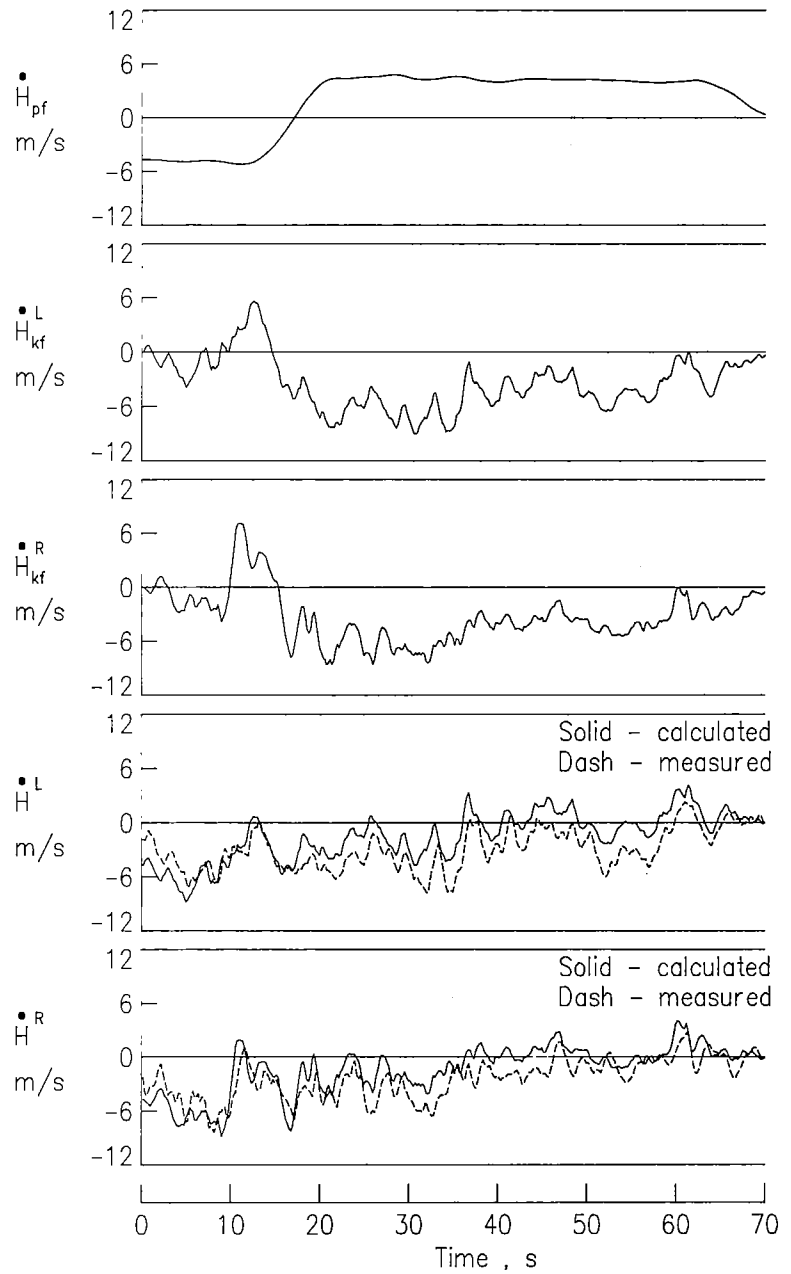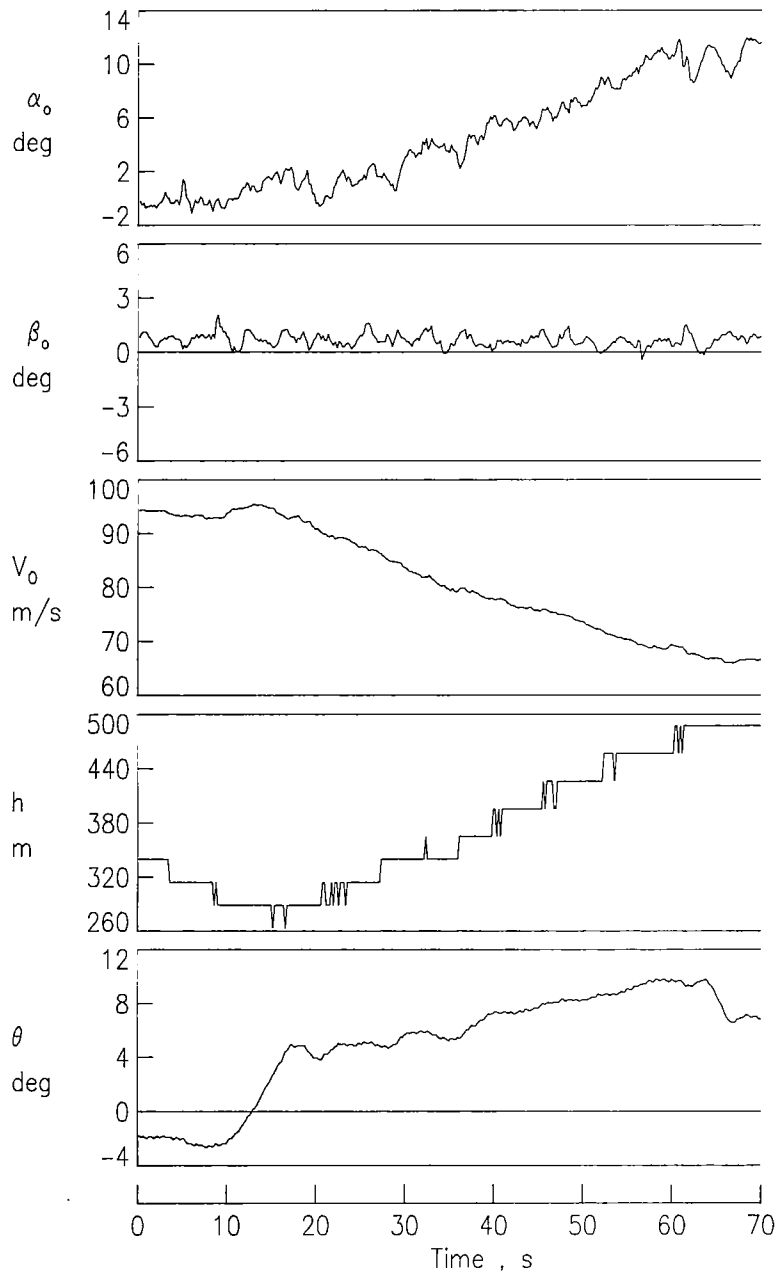Figure 9.- Test data for combined system during potential and kinetic energy exchange.
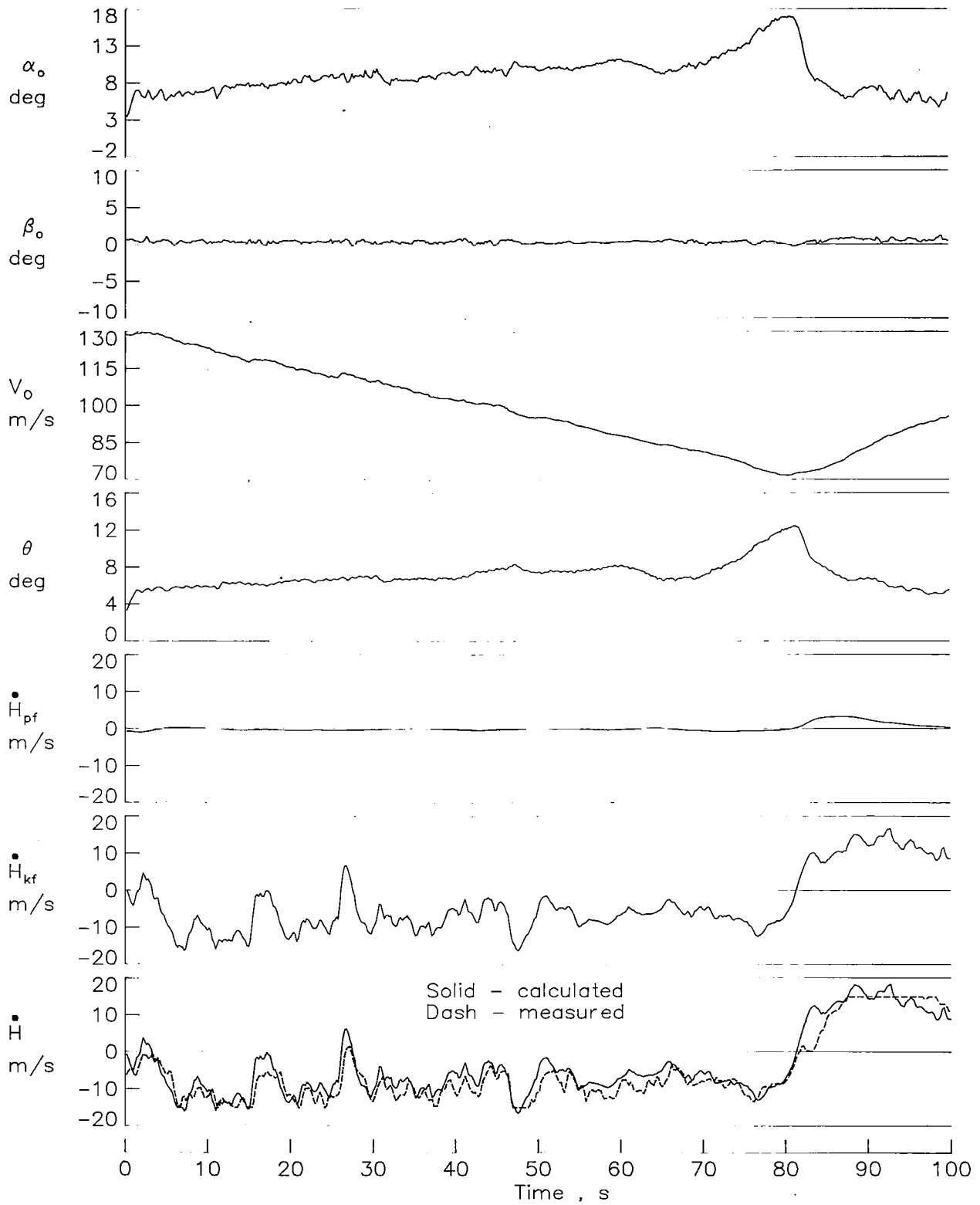
Figure 10.- Test data for combined system during kinetic energy change.
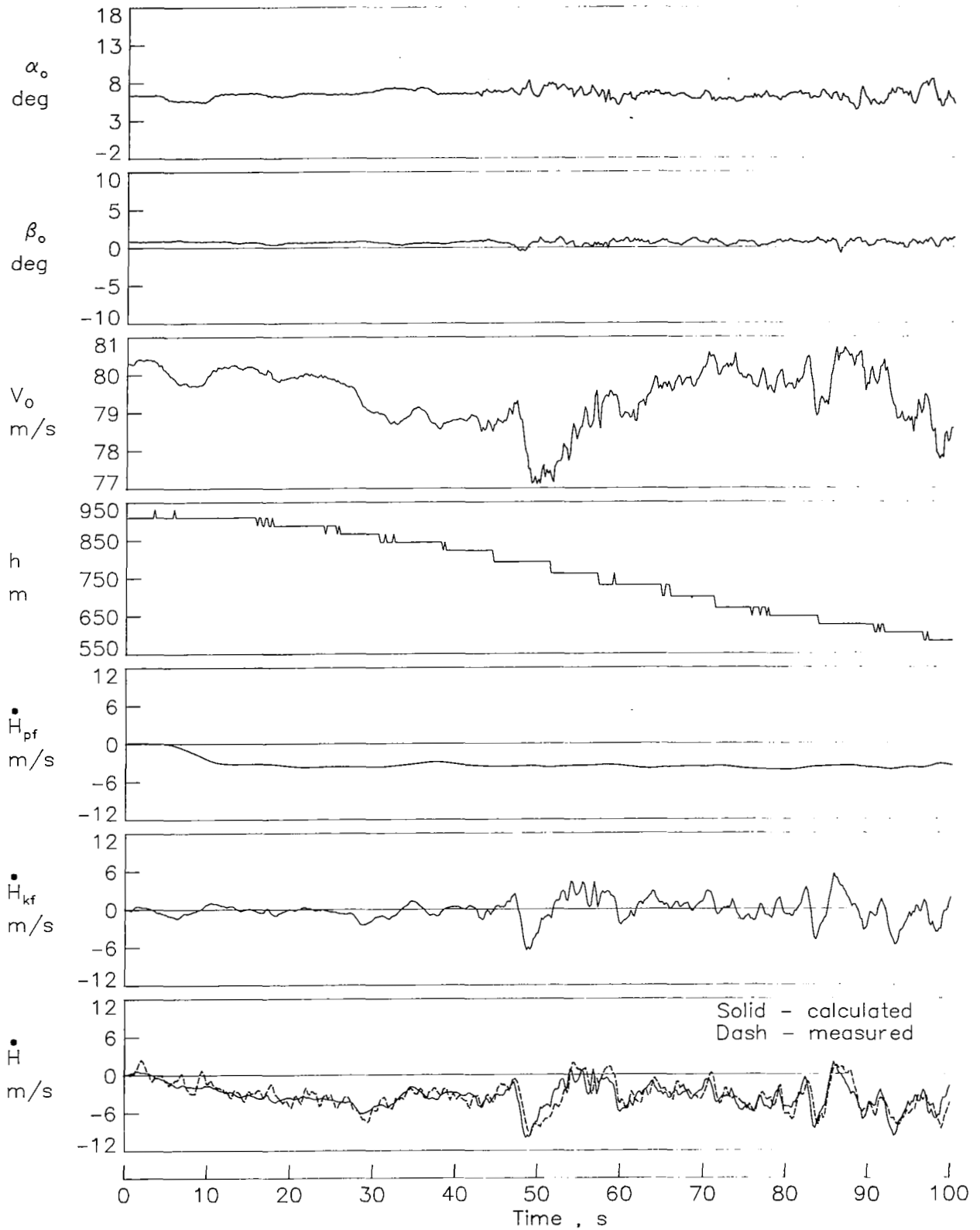
Figure 11.- Test data for combined system during potential energy change.
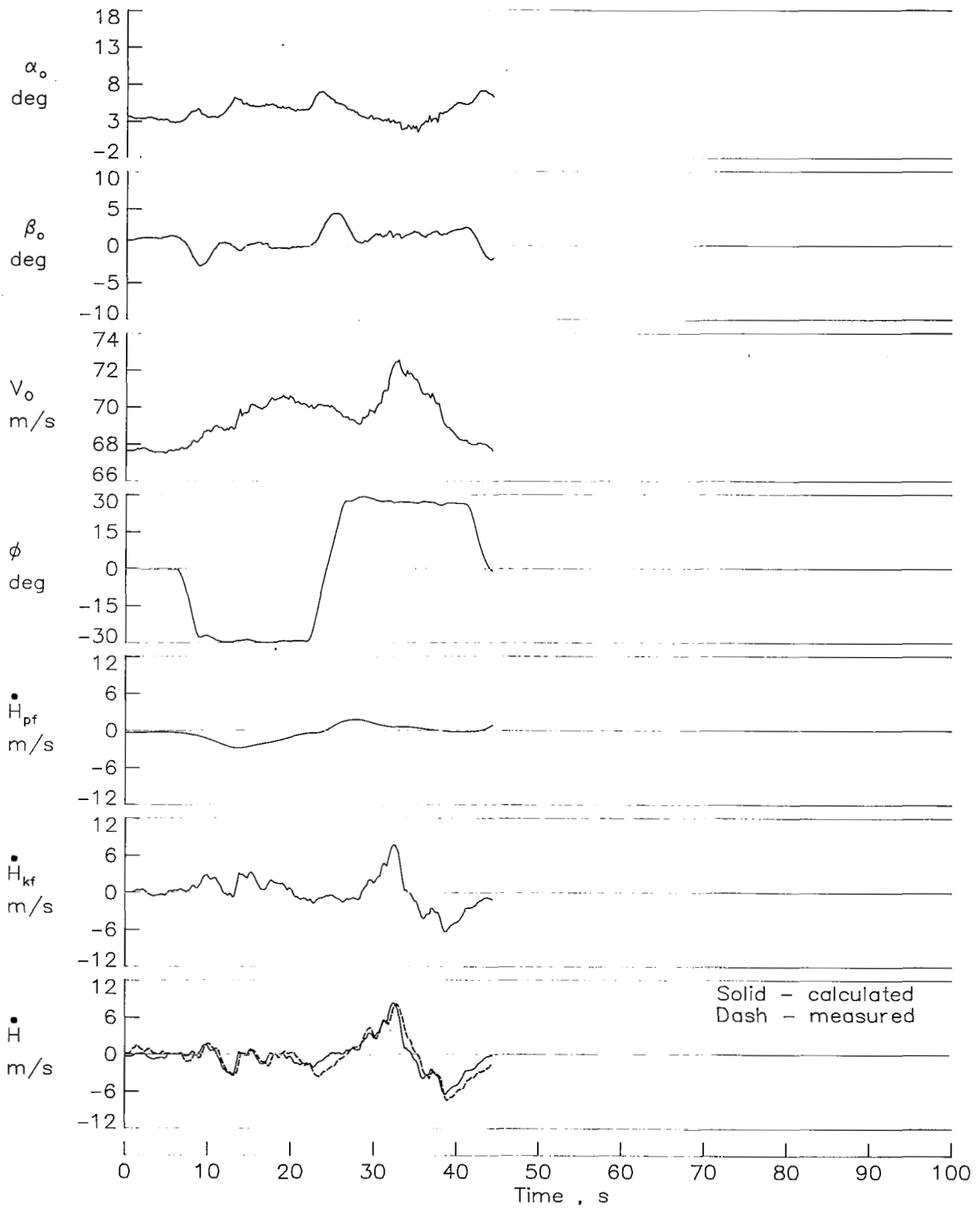
Figure 12.- Test data for combined system during roll maneuver.
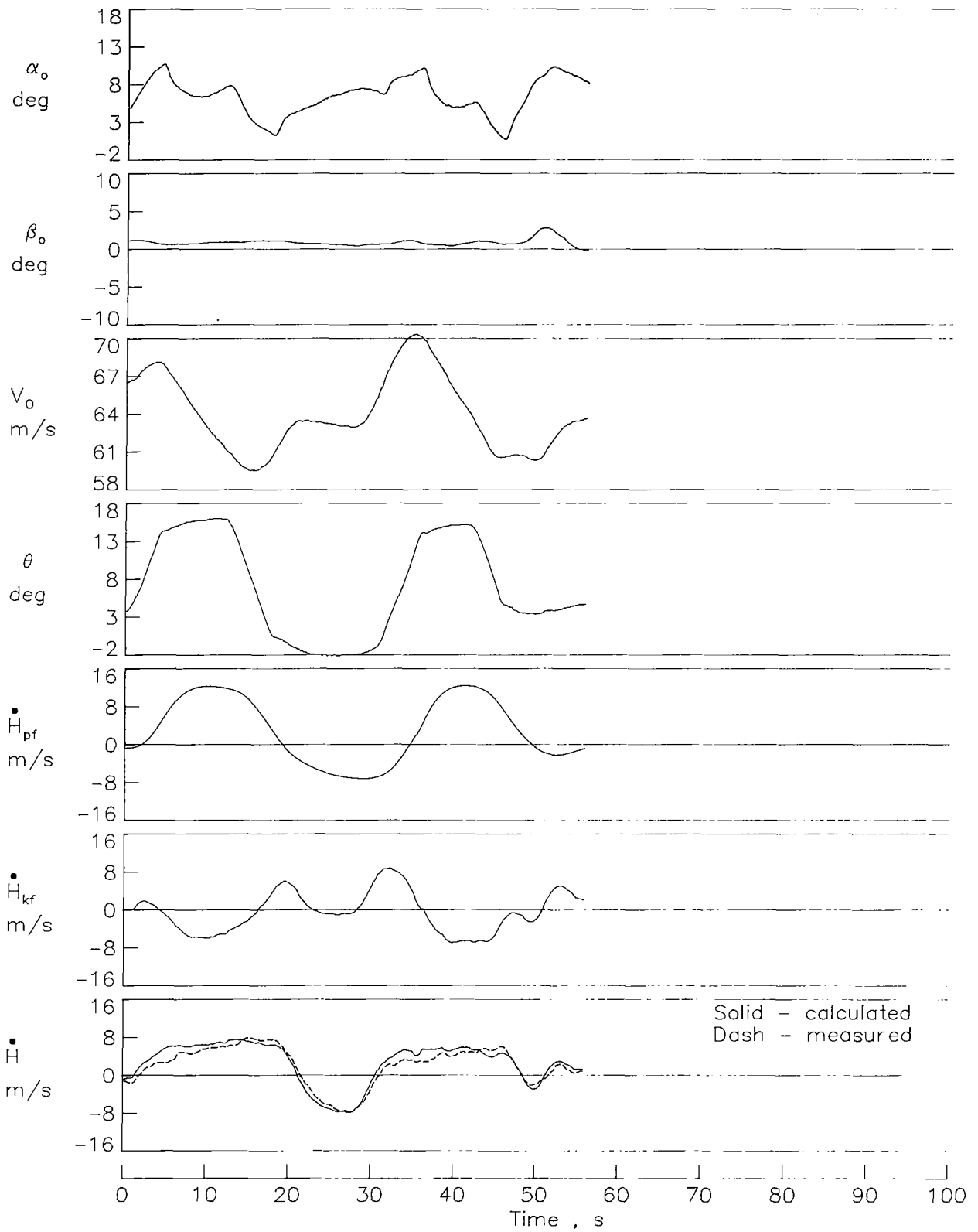
Figure 13.- Test data for combined system during pitch maneuver.
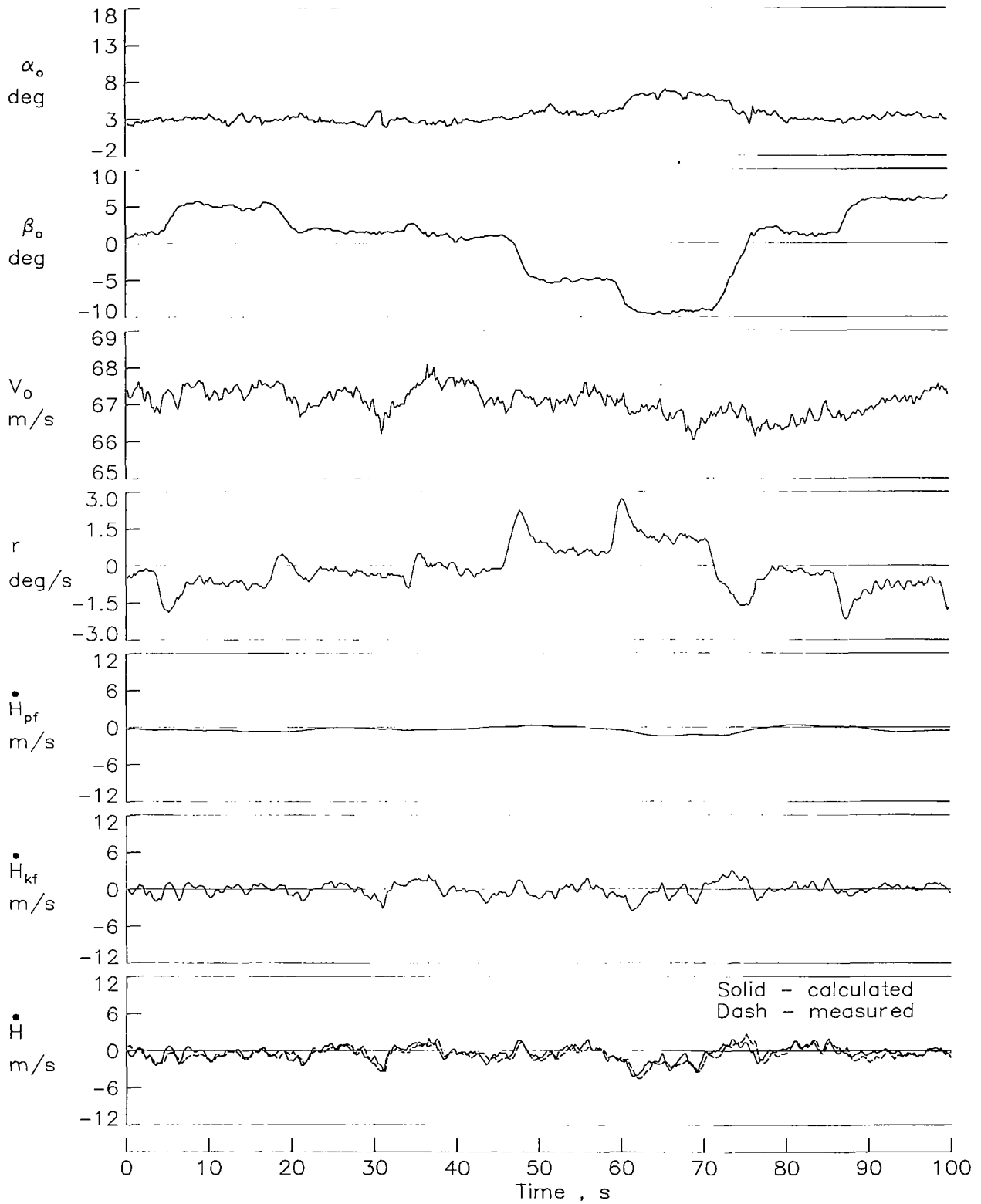
Figure 14.- Test data for combined system during sideslip maneuver.
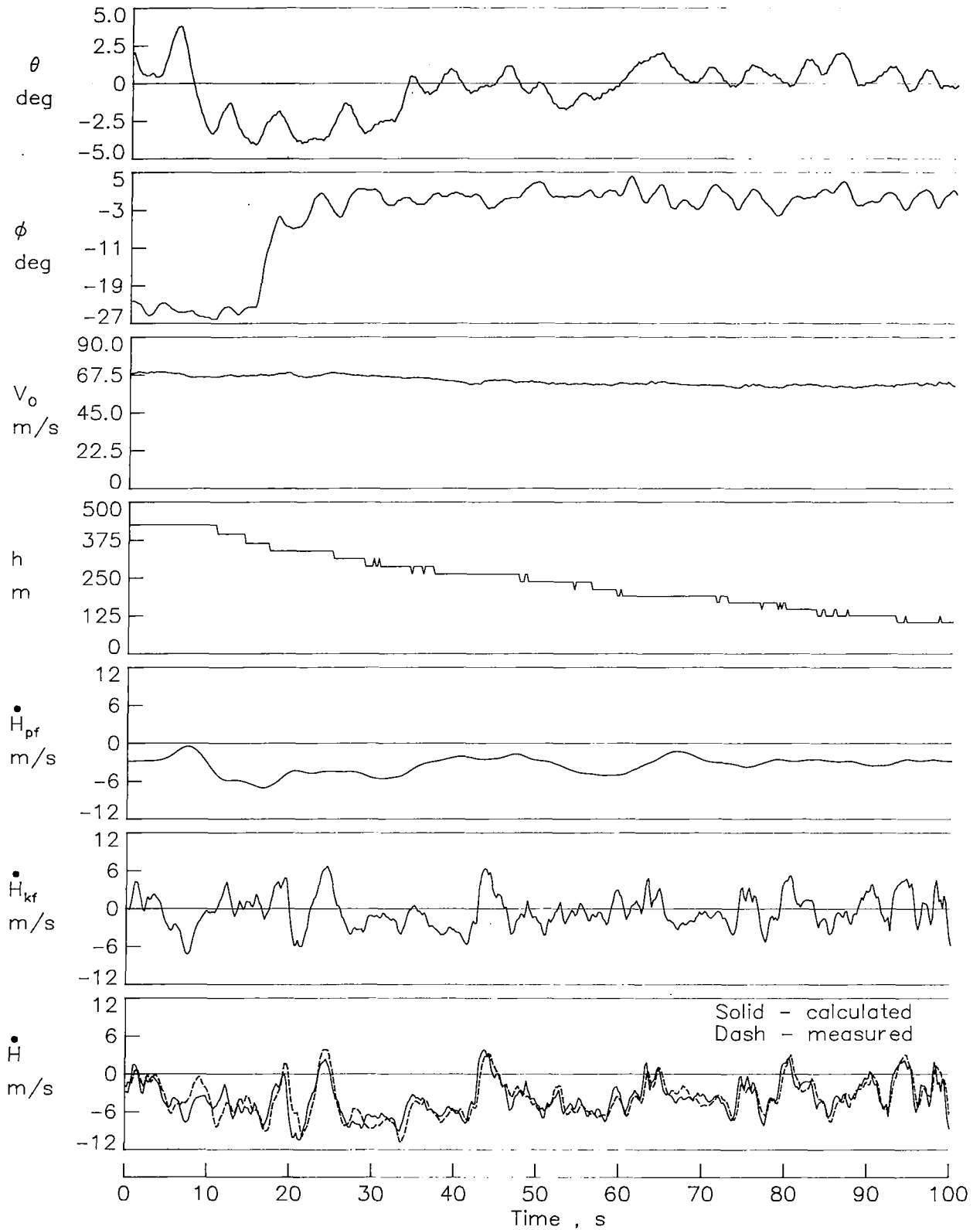
Figure 15.- Test data for combined system during landing maneuver.
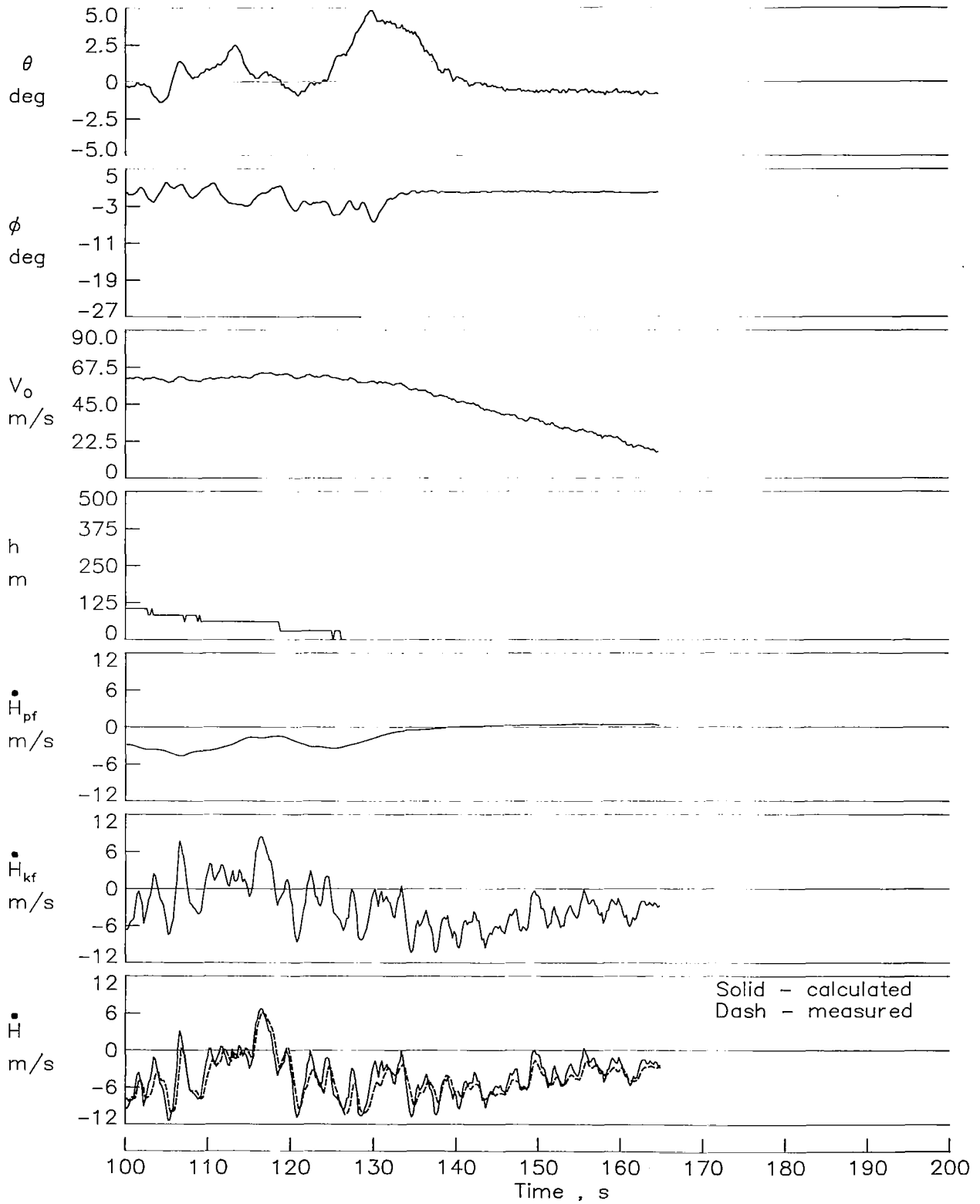
Figure 15.- Concluded.
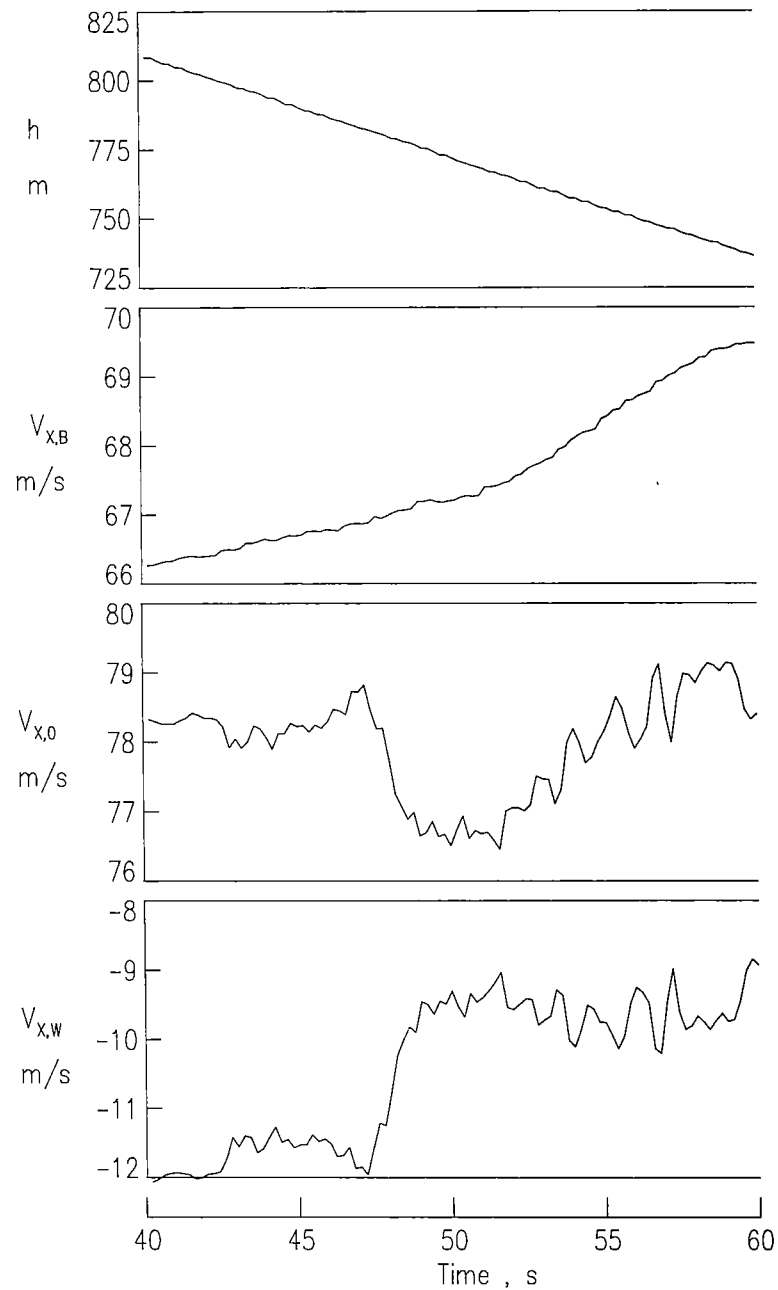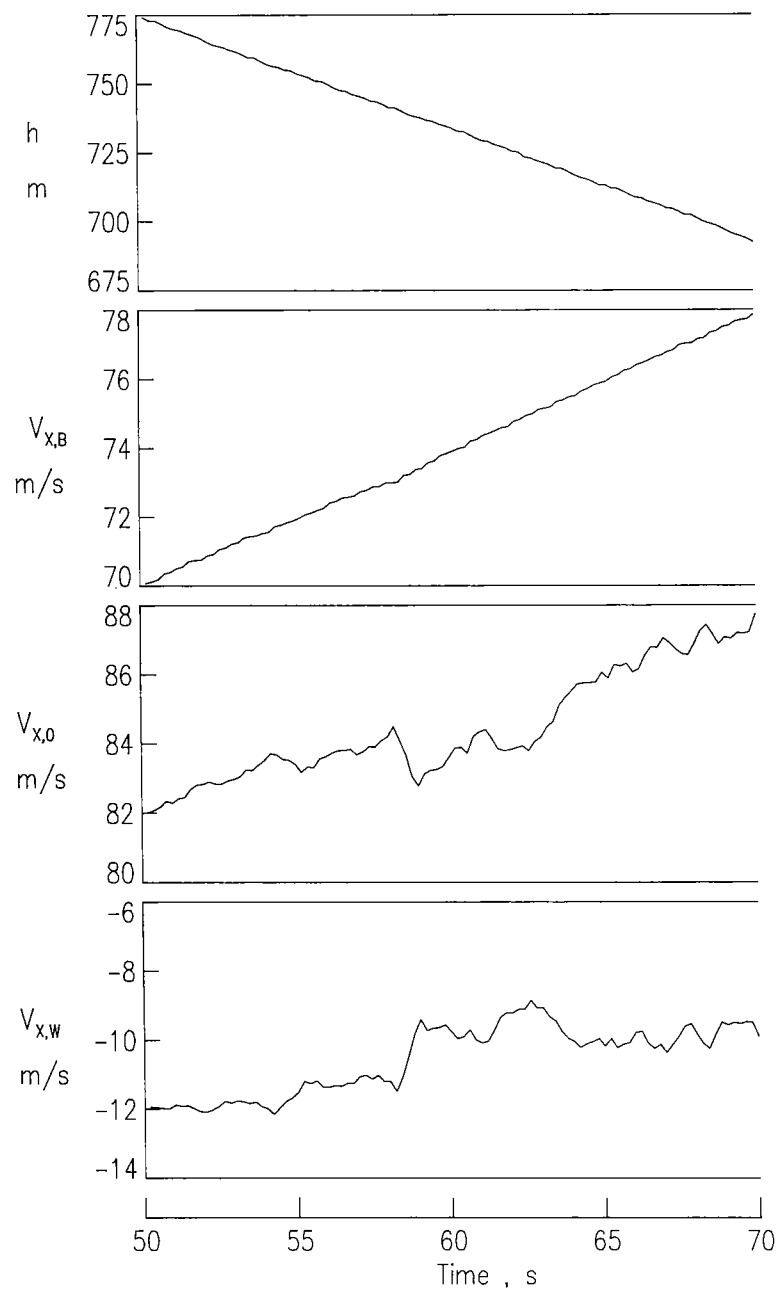
Figure 16.- Wind shear occurring in runs shown in figures 8 (left side) and 10 (right side).

Figure 17.- Test data for separate systems during potential and kinetic energy exchange.
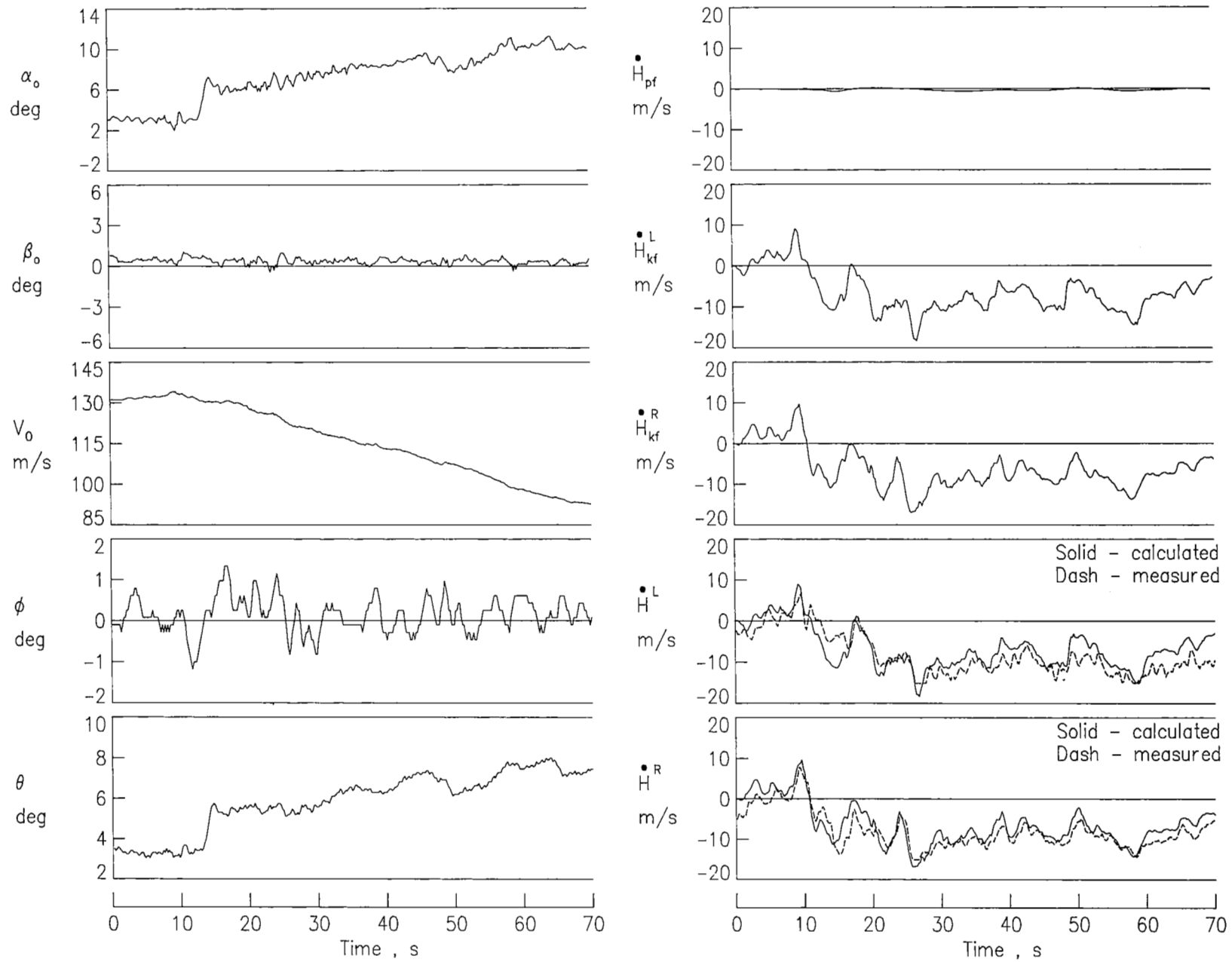
Figure 18.- Test data for separate systems during kinetic energy change.
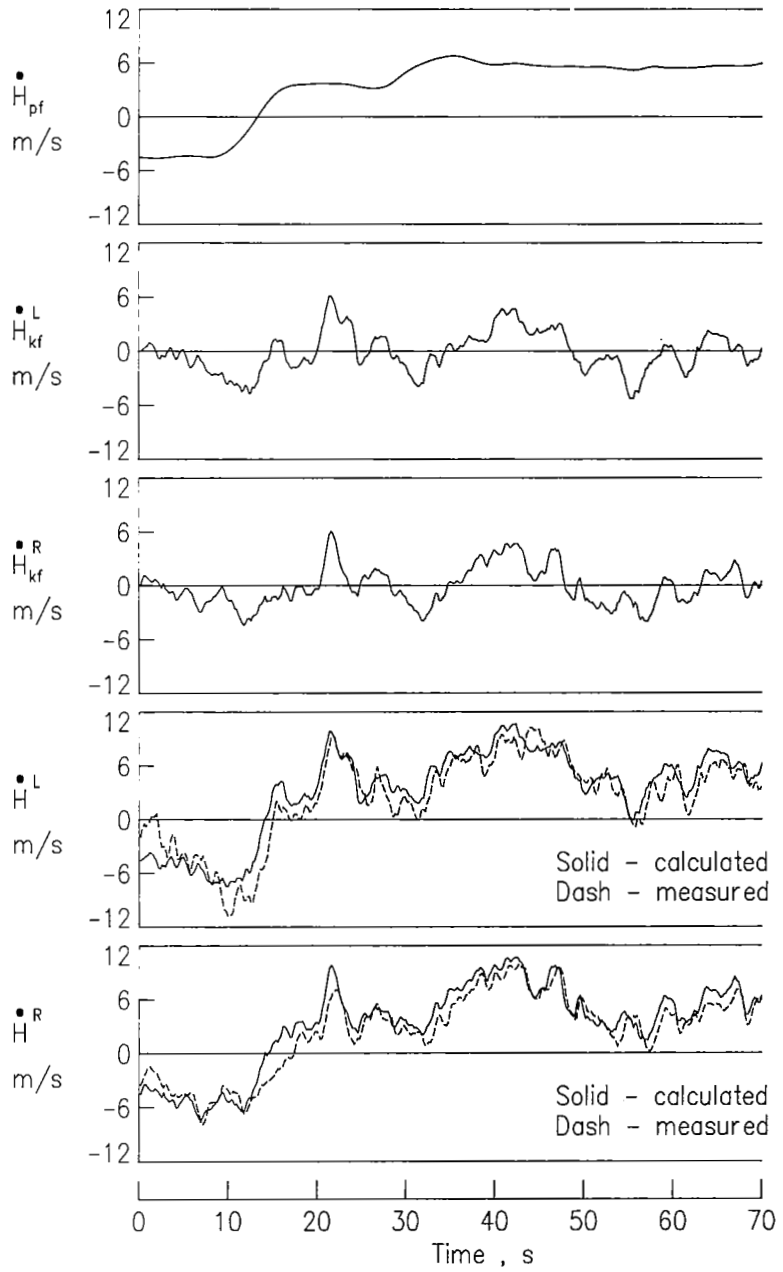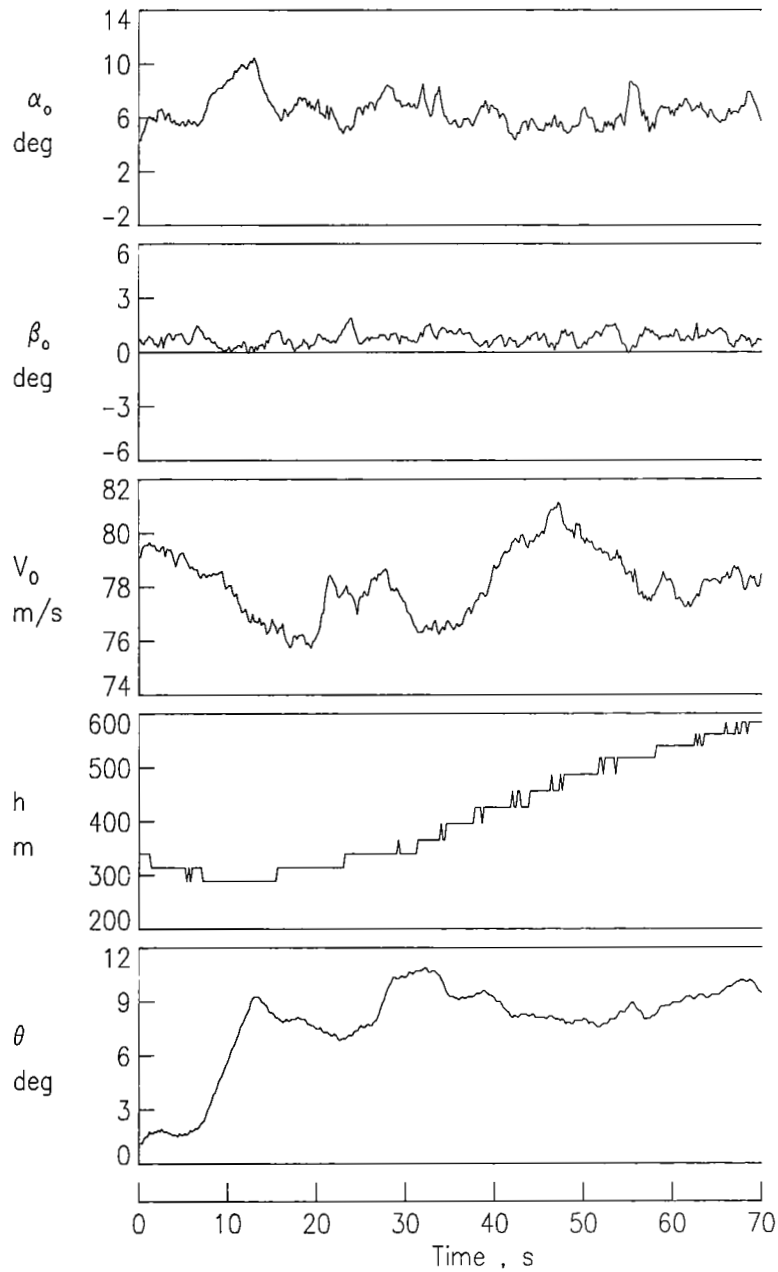
Figure 19.- Test data for separate systems during potential energy change.
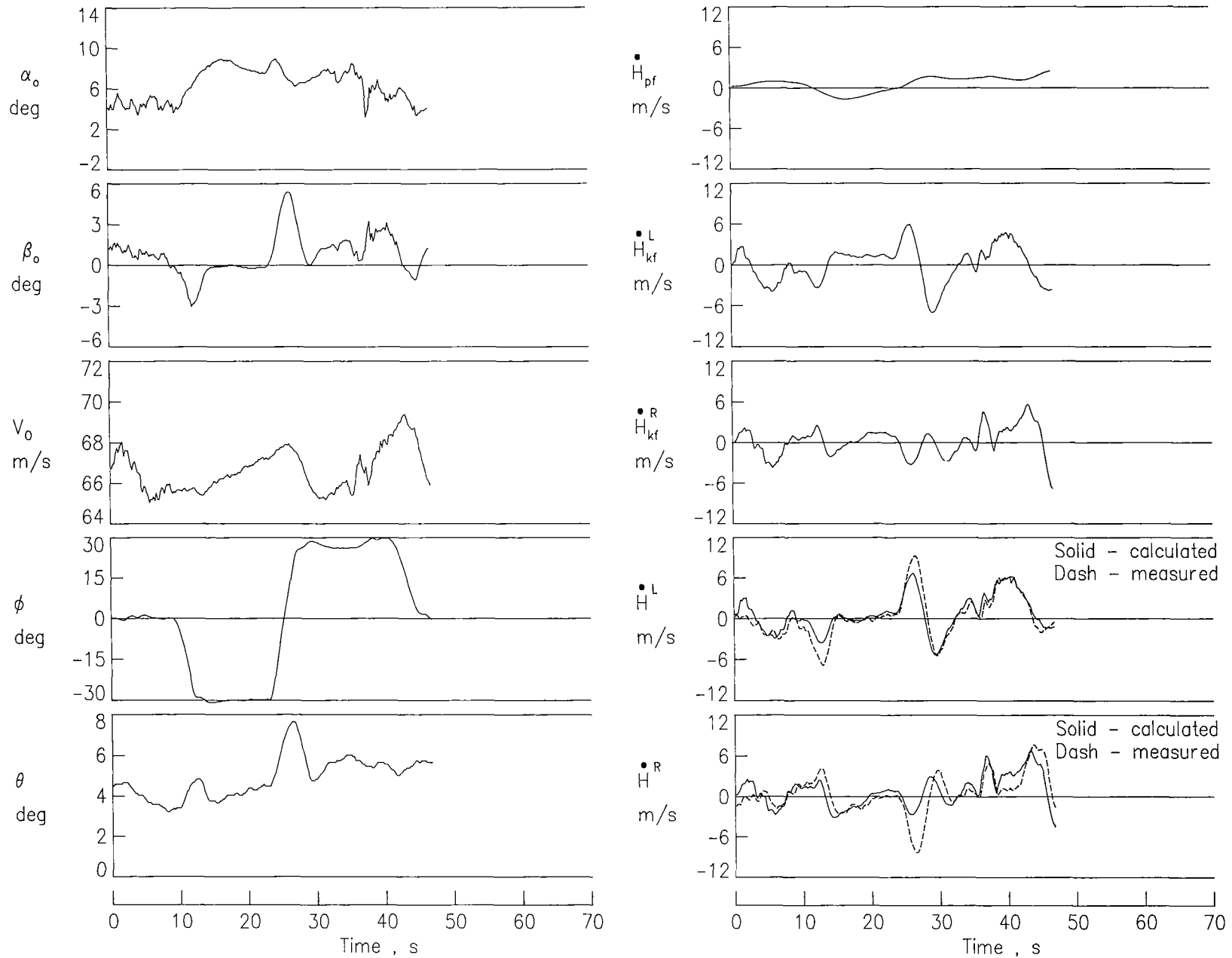
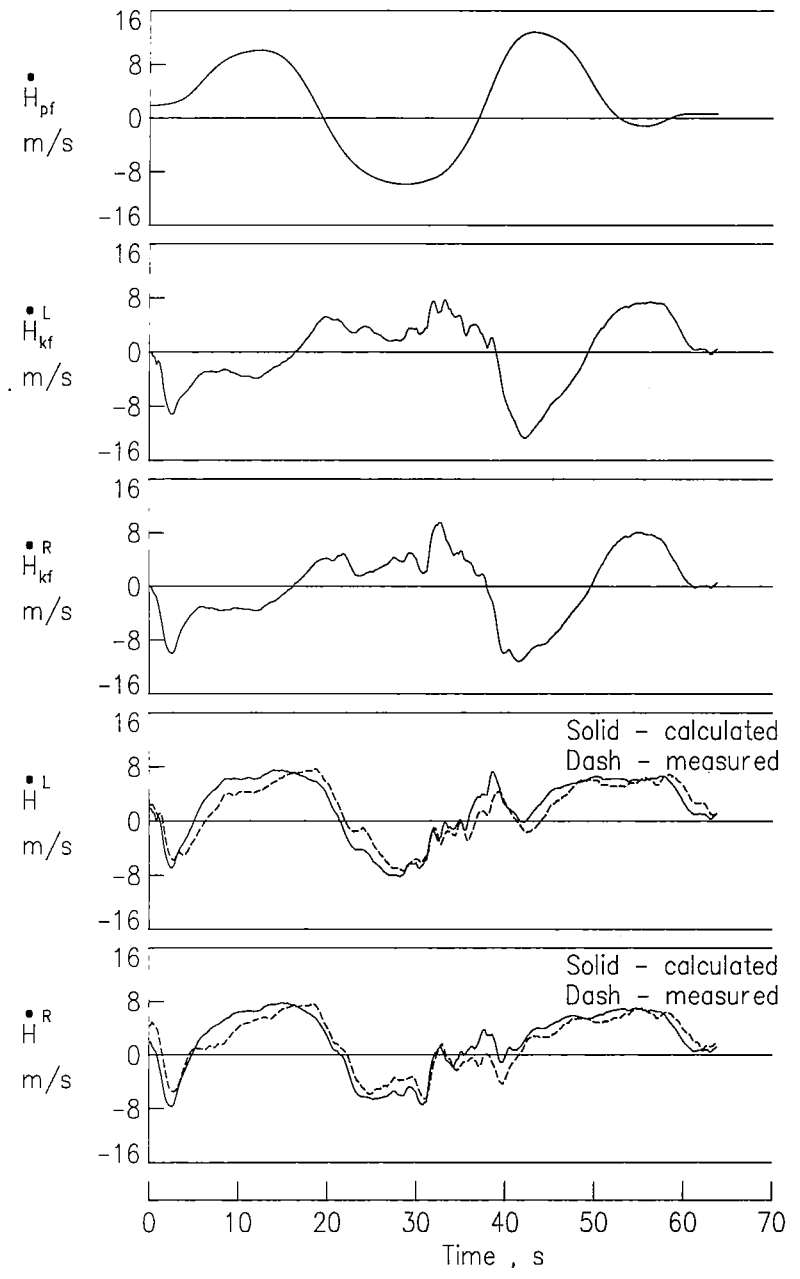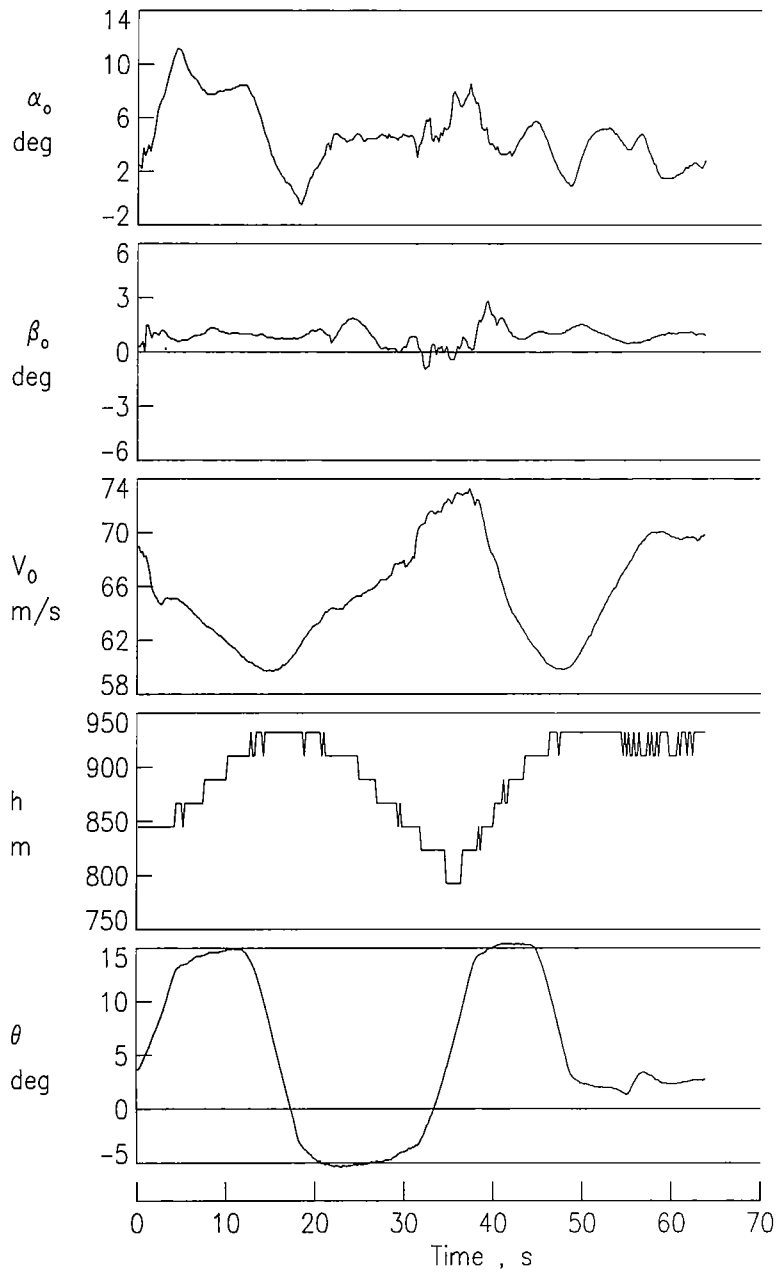Figure 20.- Test data for separate systems during roll maneuver.

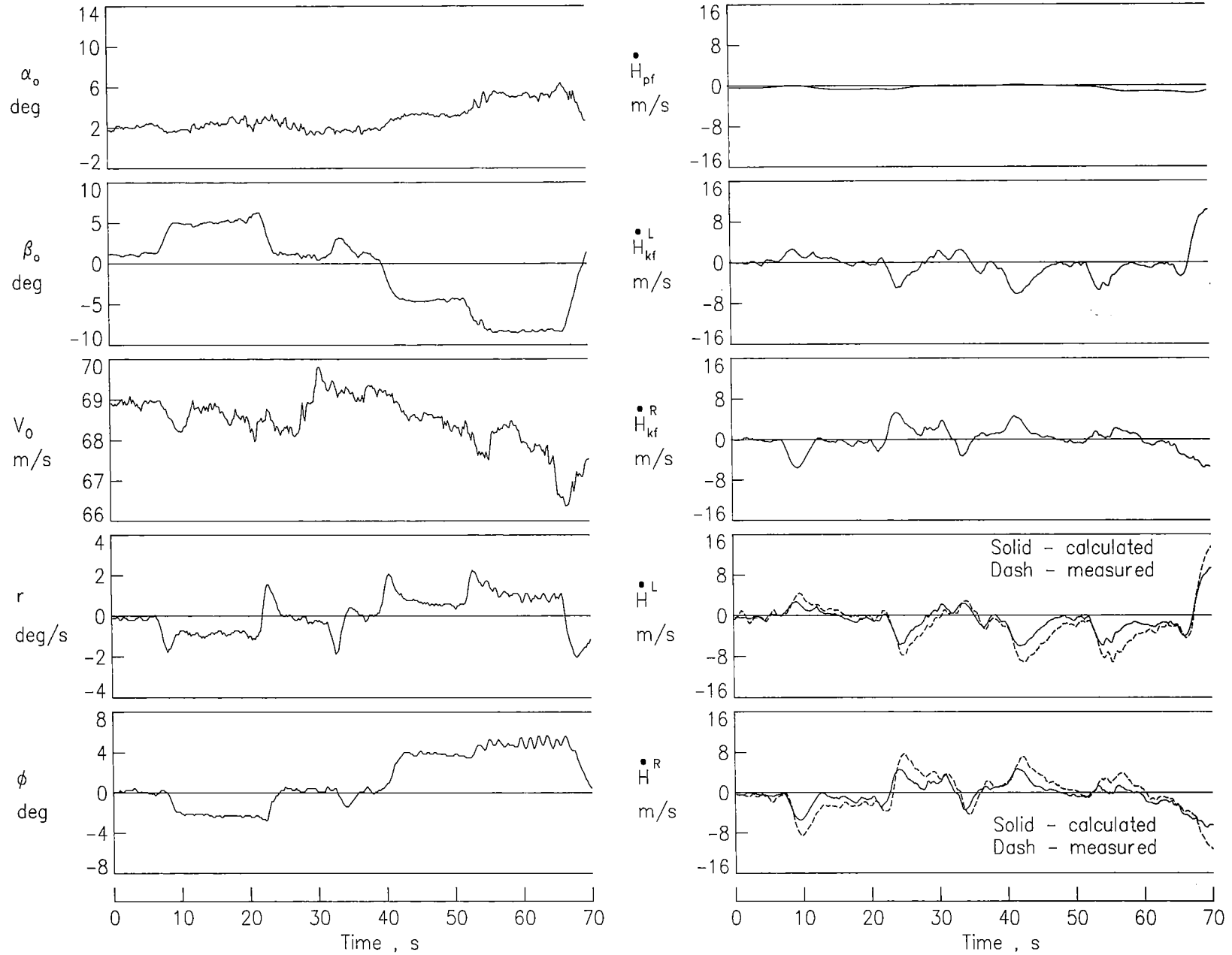Figure 21.- Test data for separate systems during pitch maneuver.

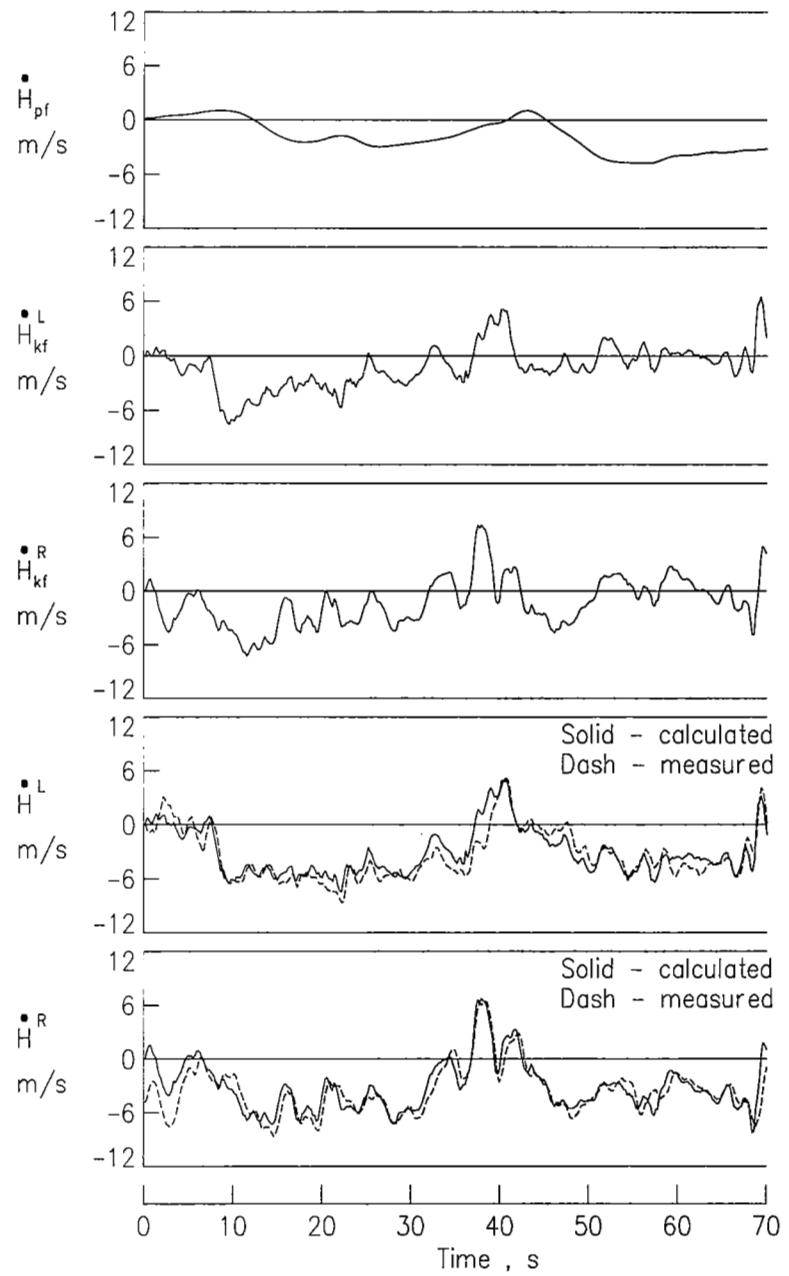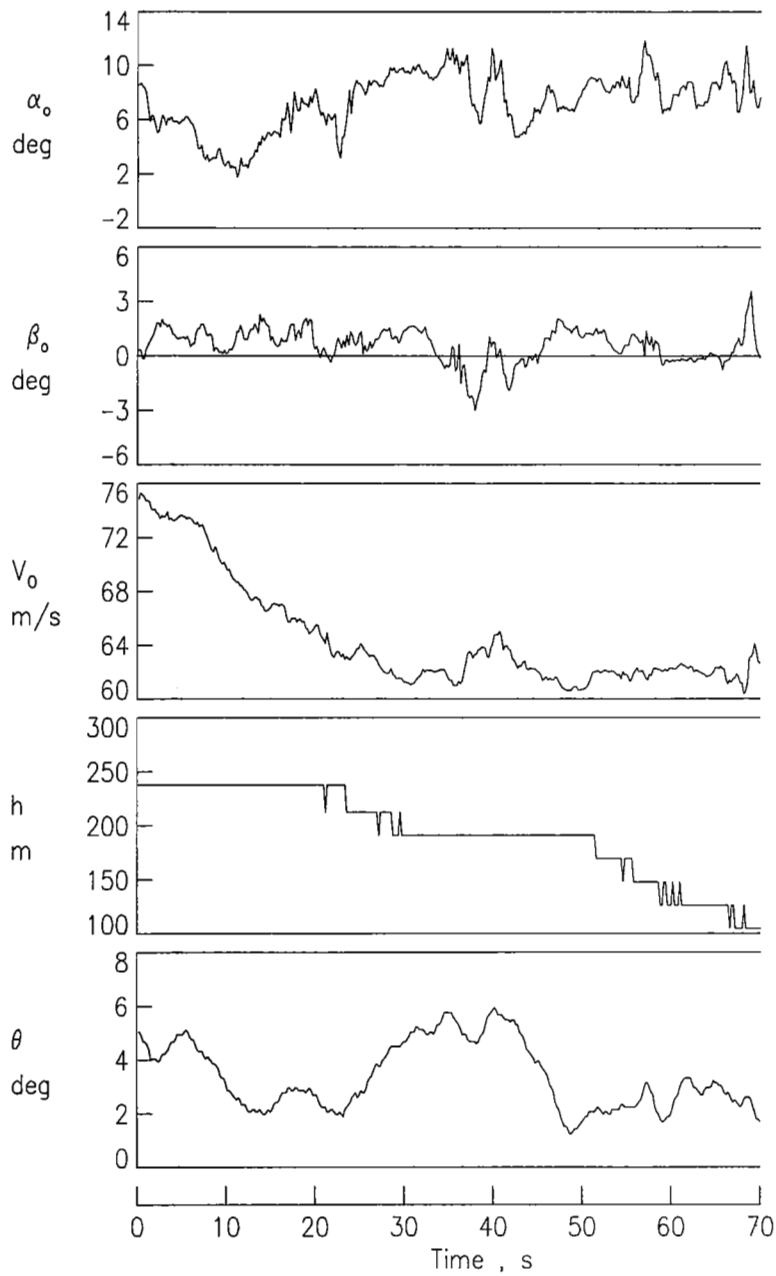Figure 22.- Test data for separate systems during sideslip maneuver.

Figure 23.- Test data for separate systems during landing.

1. Report No. NASA TP-2212	2. Government Accession No.	3. Recipient's Catalog No.
4. Title and Subtitle EVALUATION OF A TOTAL ENERGY-RATE SENSOR ON A TRANSPORT AIRPLANE		5. Report Date November 1983
		6. Performing Organization Code 534-04-13-54
7. Author(s) Aaron J. Ostroff, Richard M. Hueschen, R. F. Hellbaum, Christine M. Belcastro, and J. F. Creedon		8. Performing Organization Report No. L-15461
		10. Work Unit No.
9. Performing Organization Name and Address NASA Langley Research Center Hampton, VA 23665		11. Contract or Grant No.
		13. Type of Report and Period Covered Technical Paper
12. Sponsoring Agency Name and Address National Aeronautics and Space Administration Washington, DC 20546		14. Sponsoring Agency Code

15. Supplementary Notes

16. Abstract

A sensor that measures the rate of change of total energy of an airplane with respect to the airstream has been evaluated. The sensor consists of two cylindrical probes located on the fuselage of a transport airplane, an in-line acoustic filter, and a pressure sensing altitude-rate transducer. Sections of this report include the sensor description and experimental configuration, frequency response tests, analytical model development, and flight-test results for several airplane maneuvers. The results section includes time-history comparisons between data generated by the total energy-rate sensor and calculated data derived from independent sources.

17. Key Words (Suggested by Author(s)) Energy-rate measurement Wind shear Sensor Airplane sensor	18. Distribution Statement Unclassified – Unlimited Subject Category 06

19. Security Classif. (of this report) Unclassified	20. Security Classif. (of this page) Unclassified	21. No. of Pages 46	22. Price A03